Airborne remote sensing of concurrent submesoscale dynamics and phytoplankton

Sarah E. Lang[1], Melissa M. Omand[1], Luc Lenain[2]

[1]Graduate School of Oceanography, University of Rhode Island, Narragansett, RI 02882, USA
[2]Scripps Institution of Oceanography, La Jolla, CA 92037, USA

Key Points:

- Concurrent, airborne sub-kilometer ocean currents, sea surface temperature, and calibrated ocean color proxies are merged for the first time
- Airborne snapshots capture the impact of submesoscale dynamics on phytoplankton without spatiotemporal aliasing
- This study works towards the detection and quantification of submesoscale bio-physical mechanisms using remote sensing

Corresponding author: Sarah E. Lang, slang@uri.edu

Abstract
Submesoscale dynamics can induce significant vertical fluxes of phytoplankton, nutrients, and carbon, resulting in biological and climatological impacts such as enhanced phytoplankton production, phytoplankton community shifts, and carbon export. However, resolving these dynamics is challenging due to their rapid evolution (hours to days) and small spatial scales (1-10 km) of variability. The Modular Aerial Sensing System (MASS), an airborne instrument package measuring concurrent ocean dynamics and hyperspectral ocean color, provides a powerful tool to study the influence of submesoscale dynamics on phytoplankton and carbon. In this study, we present the first airborne observations pairing snapshots of sub-kilometer ocean velocities and their derivatives (i.e. vorticity, divergence, and strain) with concurrent ocean color and sea surface temperature. We developed airborne proxies of chlorophyll-a and particulate organic carbon, which explained about 70.7% and 65.6% of in situ variability without the need for atmospheric correction, suggesting that MASS can detect shifts in phytoplankton distributions. We also explored relationships between concurrent vorticity, divergence, strain, sea surface temperature, chlorophyll-a, and hyperspectral variables to illuminate the submesoscale processes that alter phytoplankton distributions. This study demonstrates the value of merging bio-optical and physical airborne remote sensing data to better understand the influence of submesoscale dynamics on oceanic ecosystems and organic carbon. We highlight the potential for suborbital remote sensing to quantify processes that impact phytoplankton ecosystems and carbon transport without the spatiotemporal aliasing affecting in situ sensors.

Plain language summary

Fine-scale, or submesoscale (1-10 km), processes in the ocean impact phytoplankton, with potential implications for the marine food web and ocean carbon cycle. Disentangling the impacts of submesoscale processes on phytoplankton and carbon is challenging due to their small and fast spatial and temporal scales. The Modular Aerial Sensing System (MASS) is an airborne platform capturing simultaneous measurements of submesoscale ocean dynamics and ocean color, from which phytoplankton and organic carbon distributions can be derived. The relationships between currents, temperature, and calibrated ocean color products from MASS illuminated the influence of submesoscale dynamics on phytoplankton ecosystems. This study highlights the potential of airborne remote sensing to quantify the submesoscale processes that structure phytoplankton ecosystems and oceanic carbon, without the aliasing impacting in-water sensors.

1. Introduction

Satellites and airborne sensors reveal rich submesoscale (1-10 km) variability in ocean color marked by filamentous structures, eddies, and patches arising from variations in phytoplankton concentration and pigments at the sea surface. Multi- and hyperspectral ocean color provides proxies chlorophyll-a (chl-a, indicating phytoplankton abundance) and other pigments that may reflect changes in community structure. The variability in ocean color is closely tied to physical dynamics that restructure phytoplankton ecosystems and drive active biological responses such as changes in primary productivity and shifts in community structure (Mahadevan 2016, Lévy et al., 2018, Lévy et al., 2024, Pereira et al., 2024). As the base of the marine food web and a key component of the biological carbon pump, phytoplankton are crucial to the overall health of marine ecosystems and to the ocean's role in climate (Siegel et al., 2023). New tools to simultaneously document small-scale phytoplankton distributions and corresponding physical dynamics are critical for the disentanglement of the role of submesoscale processes in ocean biogeochemistry and climate.

Submesoscale dynamics are spatially heterogeneous, quickly-evolving, and occur on similar timescales of phytoplankton growth and mortality. This presents a difficult observational challenge to characterizing the relationships between dynamics and phytoplankton distributions. The slow speed of many in situ sampling platforms (e.g. ships and autonomous vehicles) relative to time scales of variability can lead to spatiotemporal aliasing (Lenain et al., 2023). Synoptic satellite measurements can augment in situ observations, but have too coarse spatial resolutions to resolve 1-10 km length scales (e.g. NASA SWOT resolves $\sim$5 km wavelength scales; Fu et al., 2024). Airborne remote sensing capturing simultaneous measurements of ocean color and ocean physics provides a powerful tool to capture submesoscale distributions and dynamics by measuring high resolution snapshots.

Submesoscale processes are defined by a Rossby number (Ro) of O(1), length scales of about 1-10 km, and time scales on the order of hours and days (Thomas et al., 2008; McWilliams 2016). Ageostrophic dynamics at Ro of O(1) can give rise to significant vertical velocities (Mahadevan & Tandon 2006; Thomas et al., 2008), which induce fluxes of oxygen, nutrients, and carbon that lead to biogeochemical impacts (Zhang et al., 2019; Omand et al., 2015). Figure 1 outlines a few examples of mechanisms that can lead to surface phytoplankton variability. For example, upward vertical velocities, associated with surface divergence, can upwell nutrients from the pycnocline into the surface mixed layer and result in enhanced phytoplankton production at the surface in nutrient-limited regimes (Mahadevan 2016; Fig. 1a). Upwelling can also shift a deep chlorophyll maximum (DCM) from the nutricline towards the surface (Lévy et al., 2018), increasing the surface concentration of phytoplankton and increasing their exposure to light (Fig. 1b).

Increased concentrations of phytoplankton have also been observed in regions of surface convergence and downwelling. This can arise when phytoplankton with depth-keeping behavior, such as floating or swimming, can counteract downwelling (Omand et al., 2011; Taylor 2018; Lévy et al., 2018; 1c) or due to a time separation between accumulation of phytoplankton and its vertical transport (Fig. 1d). Enhanced downwelling at submesoscale fronts, dense filaments, and eddies can export phytoplankton away from light (McWilliams & Molemaker 2009; Mahadevan 2016; Fig. 1d,e) and can also export carbon that may eventually become sequestered on climate-relevant timescales (Omand et al., 2015; Freilich et al., 2024). In addition to vertical velocities, phytoplankton ecosystems transform rapidly at submesoscales due to lateral mixing and stirring (Fig. 1f), mixed layer restratification (Boccaletti et al. 2007; Fox-Kemper & Ferrari 2008; Fox-Kemper et al. 2008), submesoscale instabilities (Mahadevan 2016), and biological processes such as grazing by zooplankton (Lévy et al., 2018).

Vorticity, divergence, strain, and kinetic energy flux, calculated from synoptic velocity measurements, are useful for identifying flow regimes (Balwada et al., 2021), characterizing submesoscale dynamics (Lenain et al., 2016; Freilich et al., 2023), and quantifying energy cascades that can strengthen the mesoscale or transfer energy to dissipation scales (D'Asaro et al., 2011; Balwada et al., 2022; Freilich et al., 2023). For example, submesoscale frontogenesis is associated with strong surface convergence (negative divergence), enhanced positive vorticity, high strain, and enhanced kinetic energy flux to dissipation scales (Srinivasan et al., 2023; Barkan et al., 2019; D'Asaro et al., 2011). This surface signature is associated with an ageostrophic secondary circulation in the vertical, which induces upwelling on the light side of the front and downwelling on the dense side (Mahadevan 2016; Fig. 1e). Eddies are associated with high absolute values of vorticity and weaker strain (Balwada et al., 2021). Relationships between phytoplankton and divergence may arise due to the impacts of divergence and vertical velocities on phytoplankton growth and community structure (Plummer & Freilich et al., 2024) or between vorticity and phytoplankton due to coherent trapping by eddies (Jones-Kellett & Follows 2024).

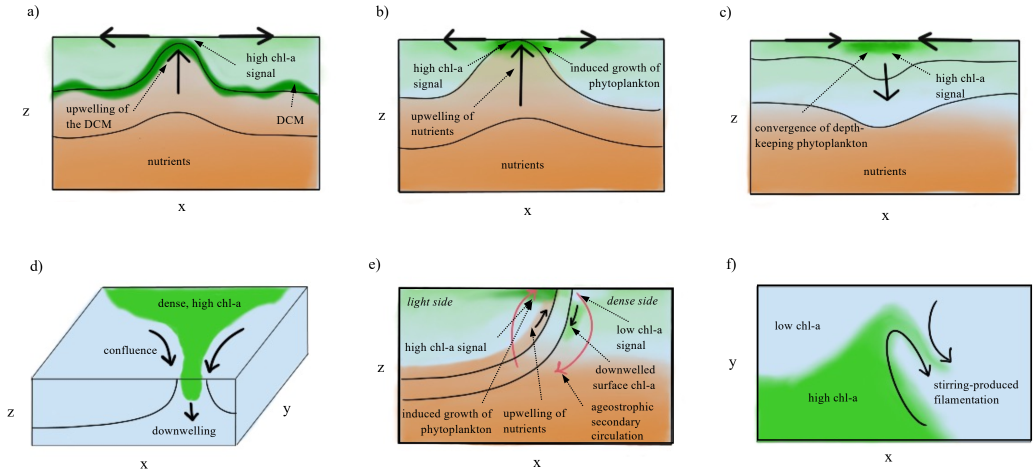

Figure 1. Schematics that illustrate a few of the mechanisms driving local surface chl-a enhancement or reduction. Upwelling of nutrients induced by surface divergence can spur the growth of phytoplankton in nutrient-limited regimes (a). Upwelling of the deep chlorophyll maximum (DCM) induced by surface divergence brings high chl-a water towards the surface (b). Surface convergence of floating or swimming phytoplankton at the surface can lead to high chl-a patches in regions of downwelling (c). Dense filaments pinching off of high chl-a water masses can converge and downwell, leading to enhanced surface chl-a associated with a vertical extent (d). Eventually, the accumulation of phytoplankton will cease and the remaining phytoplankton will be subducted or advected. Ageostrophic secondary circulation associated with submesoscale fronts can induce upwelling of nutrients on the light side of the front, spurring phytoplankton growth at the surface. This is accompanied by downwelling on the dense side of the front which can vertically transport phytoplankton away from the surface (e). Stirring of larger chl-a gradients can generate submesoscale filamentous structure.

The Modular Aerial Sensing System (MASS; Melville et al., 2016), from the Air-Sea Interaction Laboratory at the Scripps Institution of Oceanography, is a portable airborne package of instruments measuring concurrent, high resolution (256 m spatial resolution) ocean currents (Freilich et al., 2023; Lenain et al., 2023), surface waves (Lenain & Melville, 2017; Lenain & Pizzo, 2020), sea surface slope statistics (Lenain et al., 2019), internal waves (Lenain & Pizzo 2021), sea surface height (Villas Bôas et al., 2022), sea surface temperature (SST; Lenain & Pizzo 2021), Stokes drift (Lenain & Pizzo, 2020), and hyperspectral ocean color. This paper focuses on measurements of surface currents, SST, and hyperspectral ocean color from MASS. Concurrent bio-optical and physical measurements from the same airborne platform capture the relationships between fine-scale physics and biology with no temporal separation.

In this paper, we present the first airborne observations pairing concurrent snapshots of sub-kilometer ocean velocities and their derivatives (i.e. vorticity, divergence, and strain) with ocean color. We developed proxies for chl-a and particulate organic carbon (POC) using the hyperspectral data from MASS, statistical modeling, and in situ evaluation without the need for atmospheric correction. The development of ocean color methods for MASS provides an exciting opportunity to merge state-of-the-art measurements of submesoscale dynamics (Lenain et al., 2023) with high-resolution ocean color data to better understanding the submesoscale processes underpinning biological distributions and biogeochemical processes. We also explore relationships and co-occurrences between dynamical features and phytoplankton features, which illuminate the interactions between ocean physics and biology at submesoscales.

2. Experiment overview and study area

The data in this study was collected during the pilot campaign of the Sub-Mesoscale Ocean Dynamics Experiment (S-MODE), a NASA Earth Venture Suborbital-3 (EVS-3) mission. The overall goal of S-MODE is to test the hypothesis that submesoscale ocean dynamics drive significant vertical exchanges in the upper ocean (Farrar et al., 2020). Measurements from various airborne sensors are complemented by research vessels, autonomous vehicles (e.g. Wavegliders, Saildrones, Lagrangian floats, drifters, gliders), satellite data, and high resolution ocean models to diagnose and quantify the submesoscale dynamics responsible for vertical transport.

The S-MODE study site extends 200 km offshore San Francisco in the central California Current System (CCS, Fig. 2)), a region known for strong seasonal upwelling. Upwelling of cold, nutrient-rich water near the coast drives high levels of biological productivity (García Reyes & Largier 2012), and set up large gradients in properties such as temperature, salinity, and chlorophyll. Westward-propagating mesoscale eddies (10-100 km) transport water away from the coast (Amos et al., 2019) and support the formation of submesoscale features, which are ubiquitous in the CCS (Checkley & Bath, 2009). Sharp gradients in phytoplankton species have been observed across submesoscale fronts in the CCS (Taylor et al., 2012). However, relationships between fronts and phytoplankton diversity are variable and depend on the underlying mechanisms and resulting ecological responses (Lévy et al., 2015; Lévy et al., 2018).

The S-MODE pilot campaign took place between October 22 - November 8, 2021, during which MASS collected hyperspectral data over 32.55 hours and 5,997.2 kilometers. There were 7 parallel overlaps with the ship that were within 2 hours and during suitable times for ocean color data collection. Five of these overlaps occurred on October 29 (Transect A; lines A1, A2, A3, A4, A5; Fig. 2) and two occurred on October 30 (Transect B; lines B1, B2; Fig. 2). Parallel overlaps with the ship allowed for the development of empirical chl-a and POC proxies from *in situ* observations. Repeat lines increases confidence in the data collected and provides an opportunity to observe the evolution of fine-scale features.

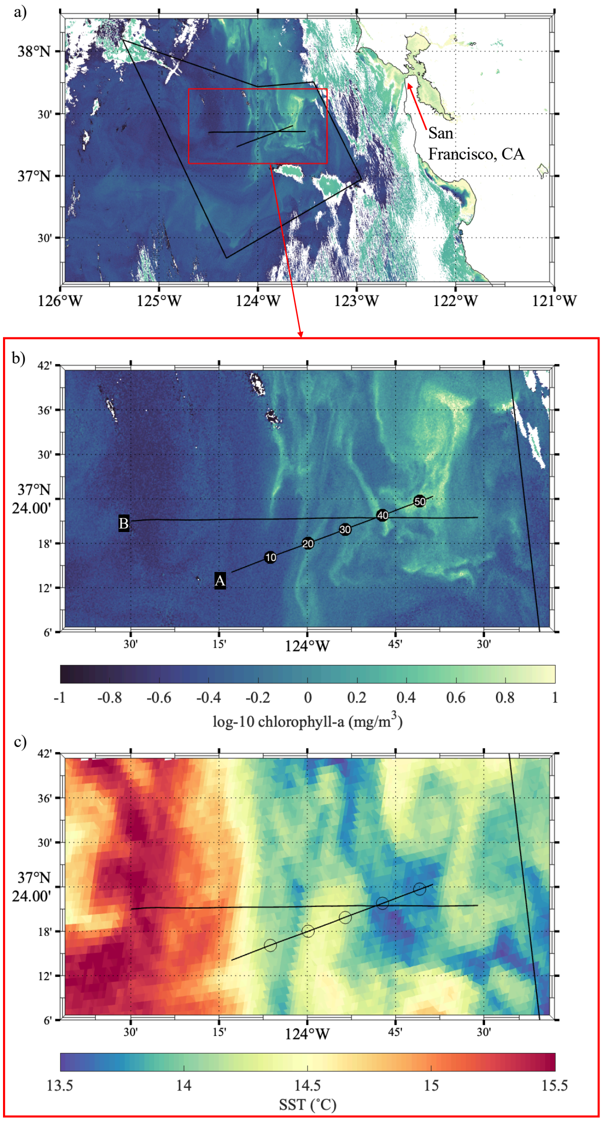

Figure 2. a) The S-MODE study region (black polygon) is overlaid on Sentinel-3 log-10 chlorophyll-a from October 29, 2021 (0.3 km resolution, time of collection (TOC): 18:44 - 18:47 UTC). Black lines indicate the repeated vessel and MASS transects. b) A zoomed-in view of Transects A and B overlaid on Sentinel-3 chl-a and b) sea surface temperature from the same day (1 km resolution, TOC: 17:01 - 18:42Z). Transect A was flown over 5 times and each line will be referred to as A1 (TOC: 19:36 - 19:57 UTC), A2 (TOC: 20:23 - 20:41 UTC), A3 (TOC: 20:44 - 21:01 UTC), A4 (TOC: 21:06 - 21:23 UTC), and A5 (TOC: 21:52 - 22:09 UTC). Transect B was flown over 2 times and each line will be referred to as B1 (TOC: 20:31 - 20:51 UTC) and B2 (TOC: 21:01 - 21:28 UTC). Flights over these transects made parallel overlaps with the ship (TOC: 12:44 - 21:29 UTC). Distance along track in kilometers for Transect A (line A2 analyzed in Sections 5 and 6) are denoted by black circles and white numbers in panel b.

3. Data collection and processing

Seawater samples for chl-a and POC (N = 149) were collected from the R/V Oceanus science seawater system at predetermined intervals during the S-MODE pilot cruise (Lang et al., 2023a). These seawater samples were used to create in situ proxies of chl-a and POC from flow-through bio-optical data. Flow-through bio-optical data were collected from a WETStar Fluorometer (Seabird Scientific) measuring chlorophyll fluorescence (excitation at 460 nm, emission at 695 nm) and a C-Star Transmissometer (Seabird Scientific) measuring beam transmittance with a 25 cm pathlength. Detailed descriptions of in situ methods are described in Lang et al. (2023b).

Airborne data considered in this study were collected at two discrete altitudes: 0.4 km ('low altitude') and 0.9 km ('high altitude'). MASS can fly underneath high altitude clouds. As long as there is still sufficient solar irradiance for ocean color retrievals, MASS can capture ocean color data at times that orbital sensors and high-altitude airborne sensors are unable. MASS is equipped with a downward looking AISA Kestrel 10 Camera, measuring upwelling radiance ($L_t(\lambda)$; λ = wavelength of interest in nm). The AISA Kestrel 10 is a pushbroom imager with a spectral range of 398.93 -1004.62 nm at a $\sim$ 3.5 nm spectral resolution and a 1024 pixel cross-track swath. Native spatial resolutions are sub-meter-scale at flight altitudes of 0.4 - 1 km. An upward looking Fiber Optic Downwelling Irradiance Sensor (FODIS) (SPECIM, SPECTRAL IMAGING LTD.) measuring diffuse downwelling irradiance ($E_d(\lambda)$) at a $\sim$ 0.6 nm spectral resolution was mounted on the top of the aircraft.

Sea surface temperature (SST) maps were produced using a Flir SC6700SLS long-wave infrared (LWIR) camera at a 1 m resolution (Lenain & Pizzo 2021, Freilich et al., 2023). Surface currents were obtained with the "DoppVis" instrument, which uses a Nikon D850 camera synchronized with a coupled Global Positioning System/Inertial Motion Unit (GPS/IMU) system to capture the spatiotemporal evolution of surface waves in visible imagery. Lagrangian mean current profiles are inferred from the modulation of the dispersion relationship by the Doppler shift velocity, (Lenain et al., 2023). Lines A2 and A3 were high-altitude flights, which is necessary for the collection of cross-swath velocity data and the calculation of 2D spatial gradients to yield vorticity, divergence, and strain (Section 6). These currents were binned to a 256 m x 256 m resolution (Freilich et al., 2023). A2 had the clearer atmospheric conditions and is the focus of analysis in Sections 5 and 6.

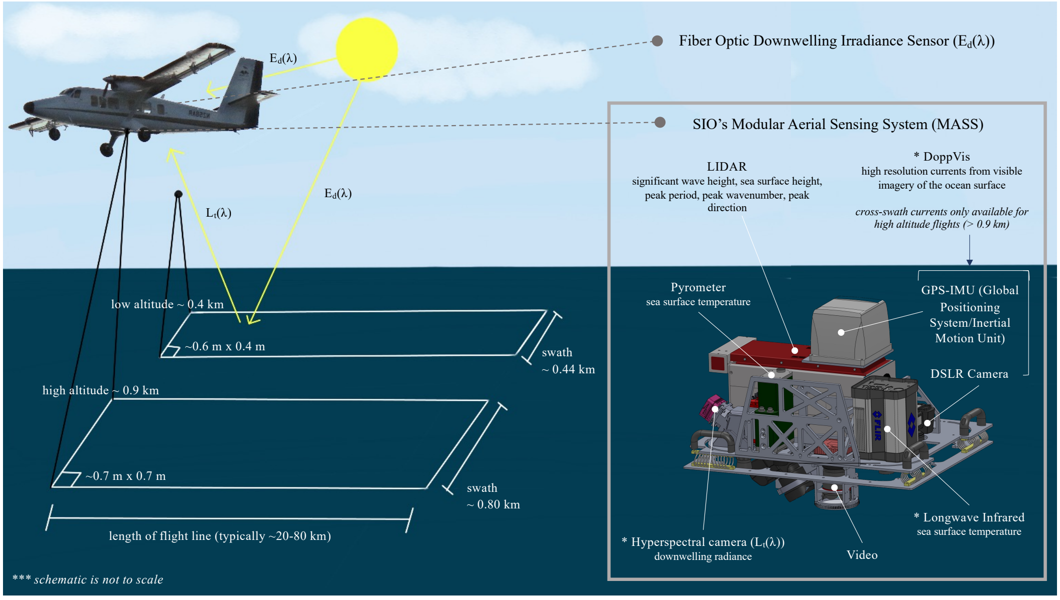

Figure 3. Schematic describing the dependency of the swath width and spatial resolution of ocean color data on the altitude of the Twin Otter aircraft (top left). The hyperspectral camera on MASS faces downwards, measuring upwelling radiance ($L_t(\lambda)$) from the sea surface and the atmosphere below. FODIS measures hyperspectral downwelling irradiance ($E_d(\lambda)$) and is mounted on the top of the aircraft. MASS is equipped with a lidar, DoppVis instrument, pyrometer, hyperspectral camera, video, and longwave infrared (right box). MASS instruments analyzed in this study are starred. Schematic is not to scale.

Hyperspectral data processing and analysis were done in MATLAB R2023b. Raw $L_t(\lambda)$ and $E_d(\lambda)$ hyperspectral data (HDR and DAT) were read in to MATLAB for each wavelength band, as well as the corresponding positional data from the GNSS/IMU sensor on the AISA Kestrel 10. $L_t(\lambda)$ pixels were spatially averaged with a 15 x 32 box (corresponding to about an 9 x 13 m resolution at 0.4 km altitude and 10 x 22 m resolution at 0.9 km altitude). Solar zenith and azimuth angles were calculated using a Solar Position Calculator in MATLAB (Mikofski 2024). $E_d(\lambda)$ data were smoothed with a 2 minute median filter and corrected with cosine corrections by the methods of Homolova et al. to account for varying solar and viewing zenith and azimuth angles (2009).

Ocean color remote sensing data typically undergoes an atmospheric correction. Atmospheric correction isolates the water-leaving radiance from the total upwelling radiance signal $L_t(\lambda)$ by removing any contributions from the atmosphere (above and below the sensor) and sea surface (e.g. glint, white-caps, background sky radiance reflected off the sea surface) (Mobley et al., 2016). This procedure also accounts for varying solar and viewing geometries, out-of-band responses, and polarization effects (Mobley et al., 2016). Atmospheric correction is a crucial step for satellite ocean color retrievals, as the atmosphere contributes ~70-90% of the total top of the atmosphere signal (Mobley et al., 2016). For low-altitude sensors, atmospheric scattering below the sensor becomes less significant.

Airborne atmospheric correction is unique to satellite atmospheric correction in its procedures and challenges. For example, ancillary atmospheric data is sometimes used to augment the estimation of the atmospheric contribution to satellite retrievals (e.g. NASA l2gen, POLYMER; Baith et al., 2001; Steinmetz et al., 2011). This data is too coarse to be used for airborne ocean color retrievals in the same way. Additionally, Cox-Munk statistics are used to estimate the glint contribution from wind waves (e.g. NASA l2gen, POLYMER; Baith et al., 2001; Steinmetz et al., 2011). These models are not applicable at the small spatial scales captured by MASS. Lastly, (sub)meter resolutions are computationally expensive because atmospheric correction is performed on individual pixels. To avoid introducing errors that would be difficult to track through a complicated and computationally expensive atmospheric correction, we evaluated if chl-a and POC could be accurately predicted from MASS without atmospheric correction. Because MASS is flying at low altitudes (0.4 - 0.9 km altitudes for MASS vs. >600 km for ocean color satellites), the atmosphere has a much smaller contribution to the total signal. Instead, we implemented cloud masking and simple sun glint corrections, used statistical methods to account for changing solar and viewing geometries, used direct measurements of $E_d(\lambda)$ to partially account for changing atmospheric conditions above the aircraft, and evaluated ocean color estimations with in situ bio-optical data.

A cloud mask was generated with RGB bands and support vector machines (SVM) following the methods of Kang et al. (2018). Cloud masks were visually inspected and compared to RGB images generated with the red (658 nm), green (555 nm), and blue (452 nm) bands of the hyperspectral data. Significant cloud coverage was detected in first and last ~10 km of the October 29th flight lines (A1-A5) by the SVM masks, and further verified by RGB images and flight logs. These regions were masked for all analyses. This comparison also indicated that the mask falsely identified some regions of high sun glint as clouds in the middle of tracks. We applied the cloud mask to all data used in modeling airborne chl-a and POC proxies (Section 4) to subset the highest quality data, but ignored the cloud mask for lines A1-A3 (clear atmospheric conditions) for following analyses.

Sun glint was partially corrected using the black pixel assumption (Gordon & Wang 1994; Mobley et al., 2016). $L_t(799)$ was selected as the near-infrared band for correction and subtracted from $L_t(\lambda)$. Very high sun glint contamination occurred on the edges of the swaths and were manually removed. This type of sun glint can be visually detected in visible bands as high radiance values that run parallel to the flight path and along the edges of the swath. This corresponded to an average of ~200 meters (~25% of the ocean color swath) along the top of high altitude flights and 80 meters (~20% of the ocean color swath) along the top of low altitude flights.

Surface reflectances ($r_{rs}(\lambda)$, sr^{-1}) were found by taking the ratio of $L_t(\lambda)$ to $E_d(\lambda)$. Data was further quality-controlled to only include data with no low-altitude clouds, during times with optimal solar zenith angles to minimize glint (< 60°), and flights with no white caps. Flight logs were useful for detecting flights with optimal conditions.

4. Chl-a and POC algorithms

Regional airborne chl-a and POC algorithms were empirically derived using multiple regression. Hyperspectral data was first matched-up with corresponding ship-based proxies of chl-a and POC at the same location and within 2 hours, yielding 740 match-ups. To reduce spatial autocorrelation detected with autocorrelation functions, the dataset was sub-sampled at an interval of 8 points, yielding 93 match-ups for multiple regression (gray highlighted points in Fig. 4). This was the shortest interval that reduced autocorrelation to be non-significant after the first lag. Chl-a and POC were estimated with multiple regression models using a 'band ratio' and ancillary airborne variables as inputs. One-minute binned flow-through bio-optical proxies of log-10 chl-a and log-10 POC were used as the dependent variables to account for their log normal distributions (Craig et al., 2012). The along-track medians of the 'band ratios' were the primary predictors of the bio-optical proxies and based on algorithms from NASA's Ocean Biology Processing Group (OBPG): $r_{rs}(486)/r_{rs}(555)$ for chl-a and $r_{rs}(443)/r_{rs}(555)$ for POC (O'Reilly et al., 1998; Stramski et al., 2008; O'Reilly & Werdell 2019). Band ratios were significantly correlated with log-10 chl-a and log-10 POC (R^2 = 56.3%, R^2 = 48.9%), but relationships varied between lines (Fig. 4 a,b) likely due to changing viewing and solar geometries.

To account for changing viewing and solar geometries between MASS overpasses, the following ancillary predictors were explored: plane heading, pitch, roll, altitude, solar azimuth angle (SAA), and solar zenith angle (SZA). Plane heading, pitch, roll, and altitude were smoothed using a 10-minute moving mean filter to avoid introducing noise into model estimates. The largest changes in these parameters occurred between flights (durations ≥10 minutes). All predictor variables were centered by subtracting the mean. The variance inflation factor (VIF) was calculated for a full set of potential predictors to test for multicollinearity. The effect of each ancillary variable on the model was evaluated with separate linear models using the band ratio, ancillary variable of interest, and their interaction effect to predict log-10 chl-a and log-10 POC. SAA was strongly correlated with SZA (R^2 = 82.0%) and was removed. Plane roll had the least significant effect on the predictions of chl-a and POC (P = 1.4e-5), and plane heading was too correlated with other parameters. Pitch, altitude, and SZA (P = 3.6e-25; P = 3.3e-12; P = 3.8e-10) were therefore selected as the ancillary predictors used to predict chl-a and POC in the models. The VIF was reduced to low values (<2). Backwards model selection and type III ordinary least squares linear multiple regression was used to predict log-10 chl-a from band ratios, plane pitch, plane altitude, SZA, and their interactions. Non-significant interaction terms ($P < 0.05$) were removed. The procedure was repeated for log-10 POC.

Chl-a and POC models were significant (chl-a: $F_{7,85}$ = 34.2, $P<0.001$, R^2 = 70.7%; POC: $F_{5,87}$ = 41.6, $P<0.001$, R^2 = 65.7%, Supporting Information Table S1, S2). Root mean square error (RMSE) and mean absolute percent error (MAPE) were low for both models (chl-a: RMSE = 0.52 mg/m^3, MAPE = 20.7%; POC: RMSE = 6.2 µmol/L, MAPE = 19.0%). Out-of-sample *in situ* chl-a and POC agreed well with model-predicted chl-a below 3.5 mg/m^3 and POC below 45 µmol/L (Fig. 4c,d).

A simple linear fit with no ancillary variables and a linear fit with ancillary variables but no interactions were also tested and compared using the Akaike information criterion (AIC, lowest value indicates best fit) and R^2. These models performed worse (chl-a: AIC = -115.5, -129.7; R^2 = 56.2%, 63.4%; POC: AIC = -130.3,-151.4; R^2 = 48.9%, 60.2%) than the original model (chl-a: AIC = -142.4; R^2 = 70.7%; POC: AIC = -160.9; R^2 = 65.6%). Homogeneity of variance was tested by plotting normalized residuals against model predictions. Normality of residuals was tested with histograms and q-q plots.

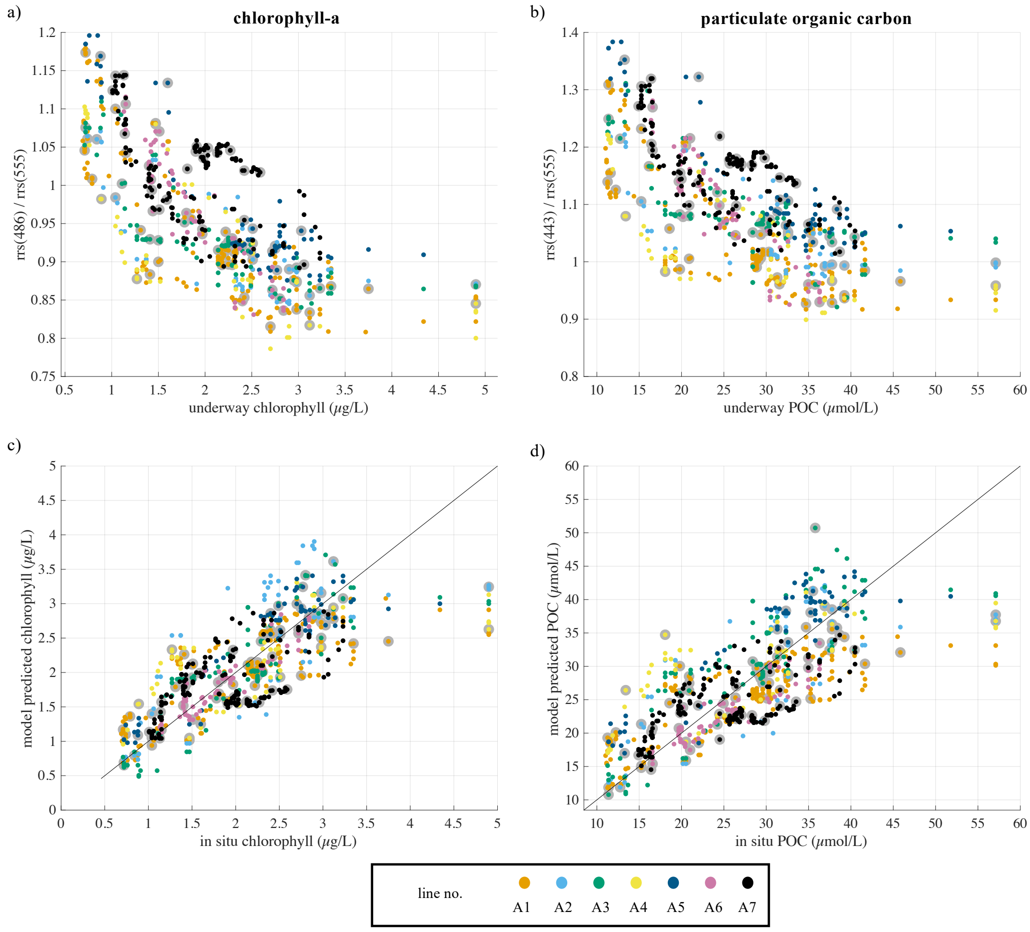

Figure 4. Ocean color parameters are plotted against corresponding in situ measurements (a,b). Airborne model predicted parameters plotted against corresponding in situ measurements (c,d). Points are colored by line number. Data points used to train the multiple regression model are outlined in light gray. 1:1 lines in solid black.

Chl-a and POC models were applied to full airborne swaths. Variability in along-track chl-a and POC at y=300 m for the three clearest and longest repeat lines (A1-A3; Fig. 5a,b) agree well with ship-based chl-a and POC (Fig. 5c), especially for in situ values less than 3.5 mg/m^3 (< 3.5 mg/m^3: R^2 = 85.6%, all: R^2 = 78.3%) and POC values less than 45 µmol/L (< 45 µmol/L: R^2 = 85.5%, all: R^2 = 80.4%). Variability also agrees well with Sentinel-3 OLCI chlorophyll-a (0.3 km resolution), albeit measuring different scales (R^2 = 66.2%).

Cross-swath chl-a, captured by repeat overpasses, shows that MASS can resolve chl-a features with variability on meter-scales (Fig. 5d-f). In the example in Fig. 5d-f, each successive flight measures a snapshot of the same feature three times in ∼1 hour and 13 minutes. The feature is detected by the ship at the same location. Overall, the spatial variability captured by the three successive overpasses agree well, although they measure different extents of the feature. The third overpass (Fig. 5f) is shifted about 50-100 m North relative to the second overpass (Fig. 5e). This shift reveals the upper extent of the low chl-a feature between 38.5 - 39.5 km (Fig. 5f). Two patches of low chl-a water are separated by a thin filament of high chl-a water that dissipates below y=200 m. There is also a high chl-a patch between 40.5 and 41 km, and the corresponding dynamical signatures are explored in Section 7.

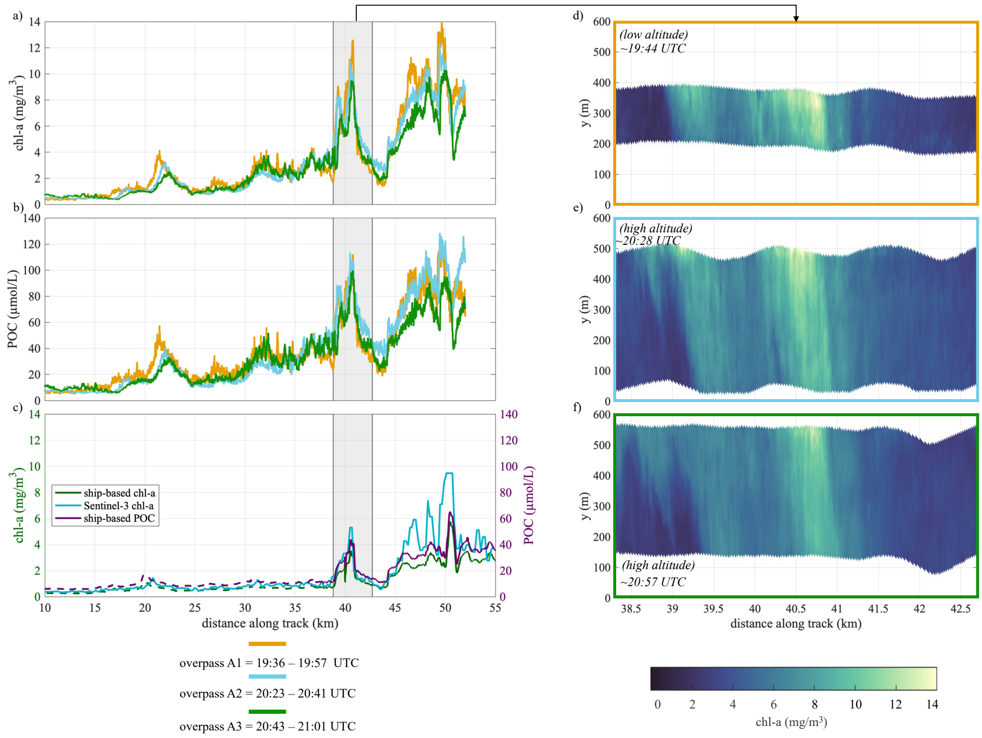

Figure 5. Along-track chl-a (a) and POC (b) for the three longest and clearest lines: A1 (orange), A2 (blue), and A3 (green). One-second binned ship-based chl-a (dark green) and POC (purple) (c). Ship based observations greater than 2 hours apart from plane observations denoted by dashed lines in (c), and ship observations within 2 hours denoted by solid lines in (c). Full swath view of high-chlorophyll feature (d-f) with central line time in UTC labeled below swath.

5. Spectral signatures from hyperspectral data

We investigated the use of the full hyperspectral data to illuminate shifts in phytoplankton community groups. Hyperspectral ocean color sensors capture continuous spectral information, allowing for the estimation of phytoplankton pigment groups from unique spectral signatures given by combinations of photosynthetic accessory pigments (Kramer et al., 2022). Principal component regression (PCR) has been used to predict phytoplankton pigments and assemblages using *in situ* phytoplankton pigment data (Bracher et al. 2015; Lange et al., 2020). It has also been used to predict chl-a in optically complex waters, where atmospheric correction is challenging (Craig et al., 2012), by separating the optical signals associated with water and its constituents (Craig et al., 2012).

Sufficient in situ accessory pigment data was not available during the pilot experiment for the validation of phytoplankton pigment-based algorithms beyond chl-a. Instead, principal component analysis (PCA) was used to decompose the spectra into signatures from different optical constituents. PC's were interpreted based on their spectral shapes. The inputs to the PCA were the along-track medians of $r_{rs}(\lambda)$ between 400 - 720 nm from A1-A5. The spectra above 720 nm becomes more heavily affected by atmospheric constituents such as absorption by water vapor or oxygen (Mobley et al., 2016). $r_{rs}(\lambda)$ was standardized by first removing the mean spectra. $r_{rs}(\lambda)$ was then normalized by the integral of $r_{rs}(\lambda)$ between 400 and 720 nm as in Craig et al. (2012) and the mean of the normalized spectra was subtracted.

Principal component 1 (PC1) explained 88.2% of the covariance in the spectra and is likely attributed to water absorption and particulate backscattering based on its spectral shape (Lange et al., 2020; Fig. 6a). PC2 explained 8.15% and is likely associated with chlorophyll-a as in Lange et al. (2020) due to dips at ~561 nm where chlorophyll-a reflects light and at ~682 nm where chl-a has its fluorescence emission peak (Craig et al., 2012; Fig. 6b). PC3, PC4, and PC5 explained 2.92%, 0.36%, and 0.09%. Although accounting for a small part of the variability, PCs 3-5 contain peaks at ~680-690 nm and ~560-570 nm likely associated with fluorescence of phytoplankton (Sathyendranath et al., 1994; Vishnu et al., 2022) and variability in phytoplankton accessory pigments. PC3 contains peaks at ~568 nm and ~685 nm (similar to PC2), PC4 contains peaks at ~500 nm and ~692 nm, and PC5 contains peaks at ~568 nm (similar to PC3) and ~692 nm. PC6 and higher may be attributed to less abundant accessory pigments or atmospheric parameters (Supporting Information Fig. S1). PC1, PC2, and PC3, which are likely associated with spectral signatures of water and its optical constituents, make up about 99.3% of the covariance in the spectra. Most covariance in the spectra being explained by in-water constituents further supports that MASS can capture meaningful ocean color information without atmospheric correction.

The relationships between PC1-5 and log-10 MASS chl-a and log-10 ship chl-a were explored for line A2 to further test if PC's were capturing the signature of in-water optical constituents. PC2 had the strongest relationship with log-10 MASS chl-a (Fig. 6e, $R^2 = 90.4\%$) and log-10 ship chl-a (Fig. 6f, $R^2 = 48.7\%$). Other lines had strong relationships between ship-based chl-a and PC2 (Supporting Information Fig. S2), but the relationship was more variable between lines than the band-ratio used to predict MASS chl-a. The relationship between MASS chl-a and PC2 was strengthened by adding PC1 and PCs 3-5 as predictors ($R^2 = 97.2\%$) and between ship chl-a and PC2 ($R^2 = 69.2\%$). Waters with high PC1 values (orange and red points in 6e) have different slopes than low PC1 values (yellow, green, and blue points in 6e) between PC2 and log-10 MASS chl-a. PC1 and PC3-5 likely strengthened the relationships between PC2 and chl-a estimated by MASS and the ship because both chl-a proxies (band ratio for MASS, chl-fl for the ship) were likely affected by optically active constituents of the water column represented by PC1 and PC3-5. In section 6, PC3-5 were used to infer shifts in phytoplankton accessory pigments, and hence, different phytoplankton community types. Since the signs of the PCA loadings are arbitrary, we determined their direction of change based on the fluorescence peak around ~680-690 nm. PC2 has an inverse relationship with chl-a and its fluorescence feature around ~682 nm is a dip. Therefore, we expect PC3-PC5 to vary directly with phytoplankton accessory pigment changes.

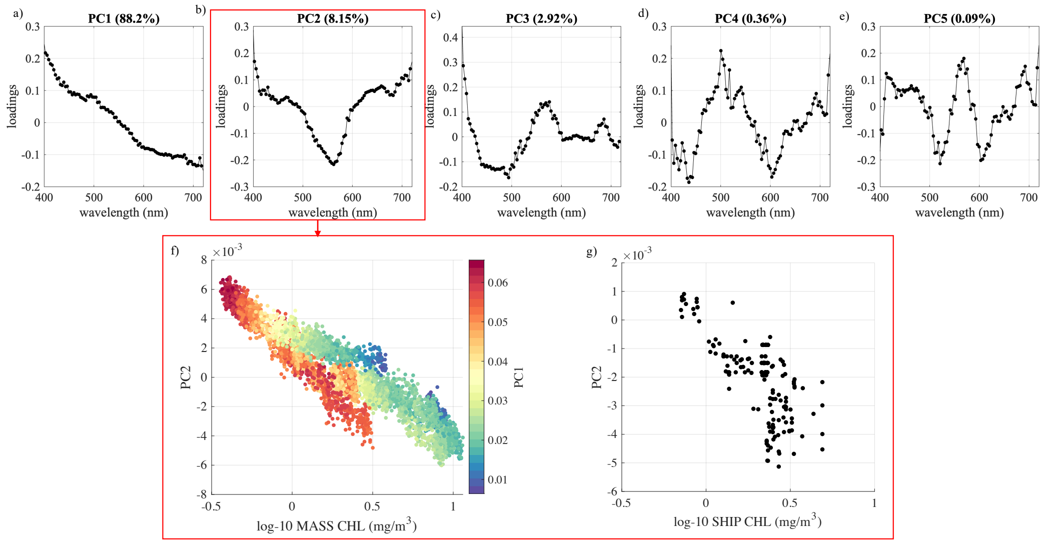

Figure 6. Loadings and percent variances for PC1, PC2, PC3, PC4, and PC5 (a-e). PC2 plotted against log-10 MASS chl-a (f) and log-10 ship-based chl-a (g) for line A2.

6. Direct observations of sea surface temperature, ocean color, and current derivatives at submesoscale features

Concurrent measurements of ocean color, SST, and currents provide the opportunity to uncover relationships between submesoscale phytoplankton variability, SST, and surface currents. Line A2 was the clearest high altitude flight and therefore the focus of the following analyses. Chl-a and SST data were re-gridded to common 10 m x 10 m grids, and the coordinate system was rotated into the along-track direction. Cross-swath zonal and meridional velocity components (u, v) from DoppVis were converted to along-track (x) and across-track (y) velocity components (u', v'), and the coordinate system was rotated into the along-track direction. Vorticity ($\zeta = v'_x$ - u'_y), divergence ($\delta = u'_x + v'_y$), and strain ($\sigma = [(u'_x$ - $v'_y)^2) + (v'_x + u'_y)^2)]^{1/2}$) were calculated from u' and v'. Vorticity, divergence, and strain were normalized by the Coriolis parameter (f = 0.89 x 10^{-4} s^{-1}).

Kinetic energy (KE) flux was also calculated from DoppVis data as in Freilich et al. (2023). Instantaneous KE flux was calculated using a coarse-graining approach (Aluie et al., 2018; Eyink, 2005; Germano, 1992):

$$\pi = -(\tau'_u v'(\bar{u'}_y + \bar{v'}_x) + \tau_{u'u'}\bar{u'}_x + \tau_{v'v'}\bar{v'}_y \qquad (1)$$

where $\tau_{ab} = \bar{ab}$ - $\bar{a}\bar{b}$ and $\bar{\cdot}$ is a top hat filter with a 1 km scale as in Freilich et al. (2023). Positive KE flux indicates a forward cascade toward smaller scales and negative KE flux indicates an inverse cascade toward larger scales.

The ship took about 9.5 hours to complete transect A (track shown in Fig. 2b, data plotted in Fig. 7a) and MASS took 20 minutes to complete line A2 (Fig. 7b-d). Fine-scale features evolved and moved quicker than the ship completed the transect. For example, the temperature front (F1 in Fig. 7b-d and ∼17 km along track in Fig. 7a) shifted ∼2.0 km along the track in the ∼5.4 hours between the ship's crossing and MASS flight. Airborne measurements avoid spatiotemporal aliasing that affects in situ platforms.

In situ temperature, salinity, and density along transect A was used to examine the surface density structure underlying the temperature gradients measured by MASS. Typically, temperature fronts are strong indicators of density fronts in this region due to the ubiquity of cold, dense, upwelling fronts in the California Current System (Mauzole et al., 2020). However during the campaign, density was dominated by salinity (Fig. 7a) due to freshwater input (e.g. precipitation, river outflow) following an atmospheric river event that occurred October 24-25th. Increased chl-a was associated with both positive (F2, F4 in Fig. 7b-d, Fig. 9, Fig. 11) and negative SST gradients (F3, F5 in Fig. 7b-d, Fig. 10, Fig. 12), indicating changes in the hydrographic and biological properties of typically colder, saltier, and higher chl-a waters sourced from coastal upwelling and surrounding waters typically warmer, fresher, and lower in chl-a.

Five regions of interest along A2 were selected to highlight fine-scale features observed by MASS (F1-F5 in Fig. 7, Fig. 8, Fig. 9, Fig. 10, Fig. 11, Fig. 12). F1 is a sharp SST front associated with a forward kinetic energy cascade of around 2 x 10^{-6} $m^2 s^{-3}$ to smaller scales (Fig. 7b,d) and peaks of vorticity, convergence, and strain on the dense (warm side) of the front (Fig. 8a, d-f). These dynamical signatures are not associated with a chl-a gradient, but are associated with a sharp decrease in PC4 and slight increases in PC3 and PC5 (Fig. 8b-c). Meter-scale figures on the cold side of F1 (blue dots at $y \approx 500$ m; Fig. 8a) denote marine mammals breaking up a diurnal warm layer to breathe. F2 is a patch of warm SST and high chl-a with a peak in PC3 (Fig. 9a-c). This patch contained meter-scale, warm filamentous features between 22-23.5 km, which are smaller than the scale captured by velocity data (Fig. 9g). Chl-a and SST anomalies were calculated by subtracting background chl-a and SST fields, calculated from 300 m x 300 m Gaussian smooths, from total chl-a and SST. Warm SST anomalies were associated with positive chl-a anomalies and cold SST anomalies were associated with negative chl-a anomalies (Fig. 9g). F3 is a patch of warm SST, high chl-a, decreased PC4, and increased PC3 and PC5 in a region of strong convergence (Fig. 10a-c,e). F4 is a SST and chl-a front with high chl-a, increased PC3, and decreased PC4 on the cold side of the front and no strong dynamical signatures (Fig. 11). The R/V Oceanus left a streak of cold water in its wake due to the mixing of a shallow diurnal warm layer (Fig. 11a). There is no wake in chl-a, suggesting that the chl-a concentration is homogeneous over the depth range mixed by the ship (Fig. 11b). F5 is a patch of warm, high chl-a water associated with peaks in PC3 and PC5, dip in PC4, and surface divergence (Fig. 12a-c,e).

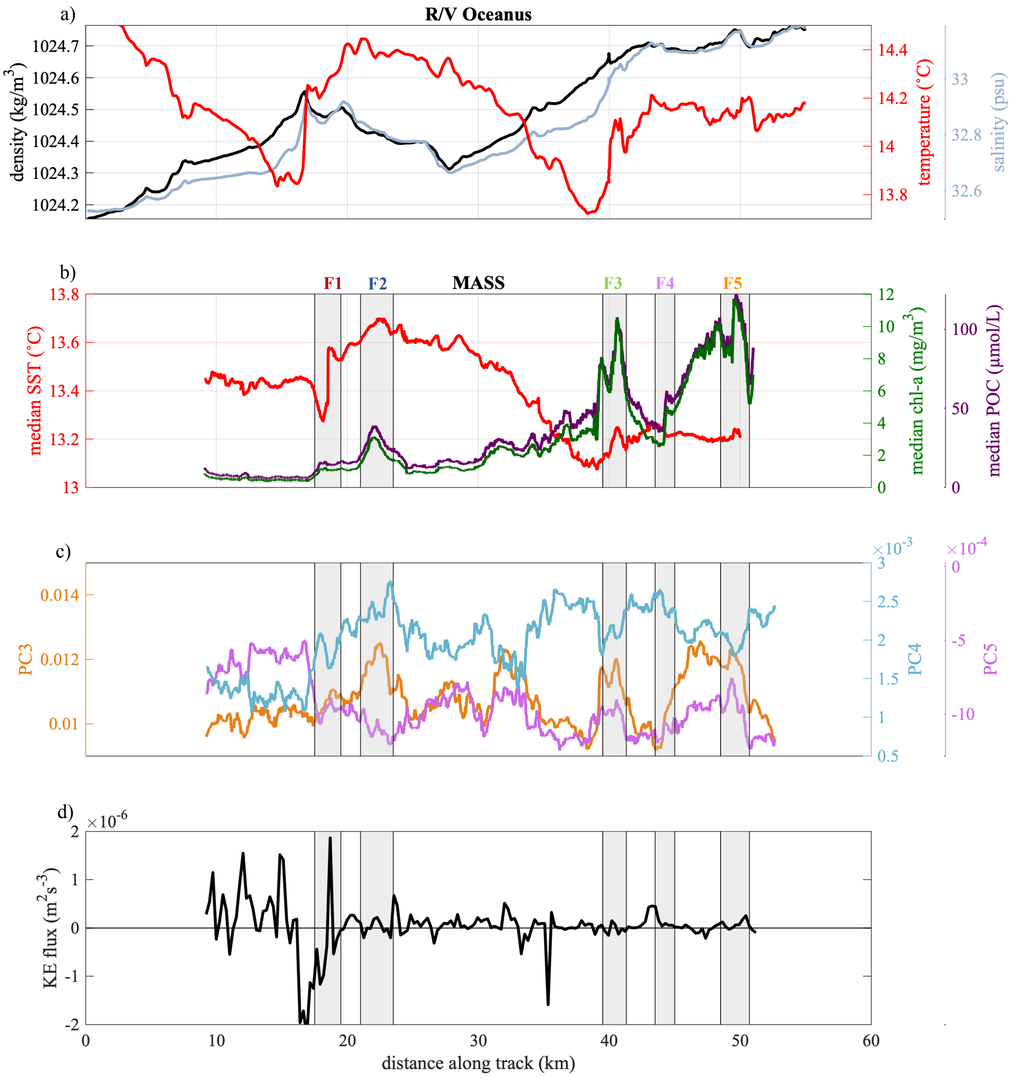

Figure 7. In situ (black), salinity (gray), and temperature (red) measured by the R/V Oceanus plotted against distance along the track (a). SST (red), chl-a (dark green), and POC (purple) plotted against distance along track (b). PC3, PC4, and PC5, representing spectral shifts likely associated with phytoplankton community shifts, plotted against distance along track (c). Kinetic energy flux plotted against distance along track (d). Five features of interest plotted in Fig. 8, Fig. 9, Fig. 10, Fig. 11, and Fig. 12 denoted by gray shaded regions (b-d).

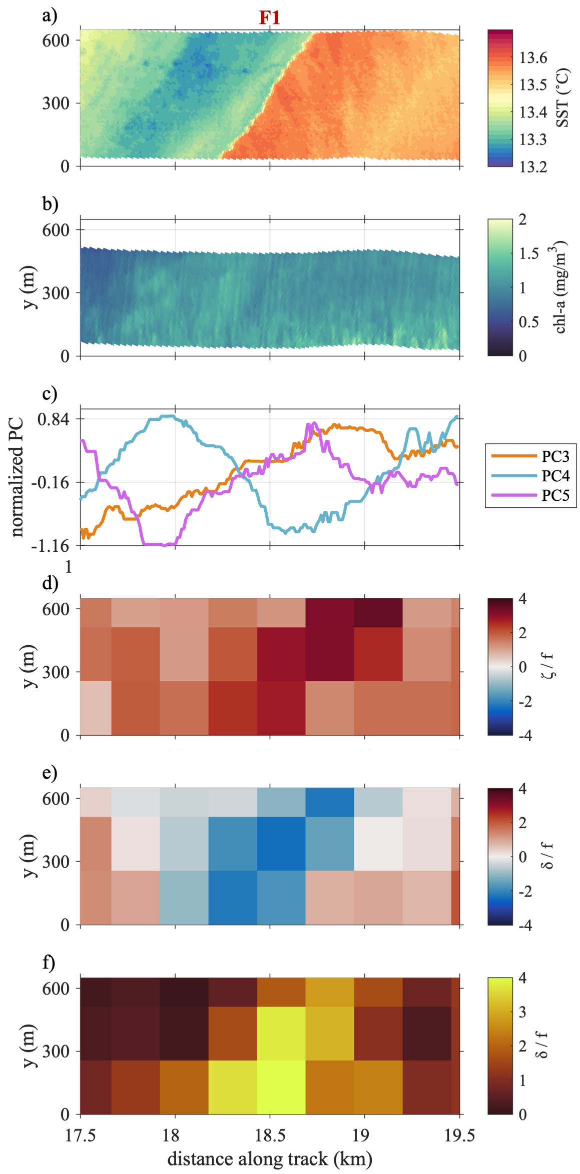

Figure 8. Full swath SST, full swath chl-a, along-track PCs 3-5, full swath vorticity, full swath divergence, and full swath strain plotted against distance along track for first feature of interest, F1. Vorticity, divergence, and strain normalized by Coriolis parameter.

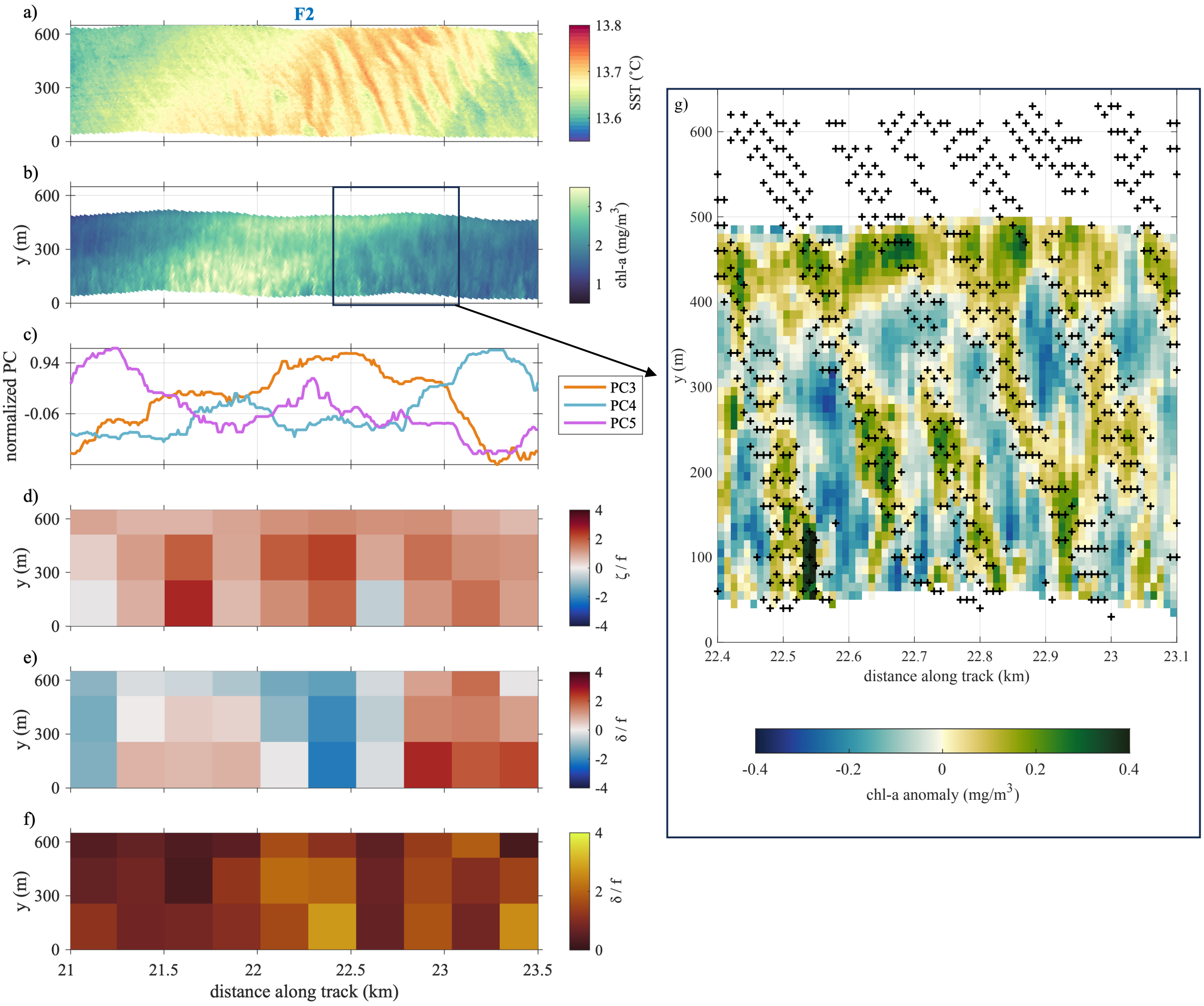

Figure 9. SST, chl-a, PCs 3-5, vorticity, divergence, and strain as in Fig. 8 for F2 (a-f). Chl-a anomaly between 22.4 km and 23.1 km, at location of colocated chl-a and SST 'finger-like' structures. Location of positive SST anomaly denoted by + overlain (g).

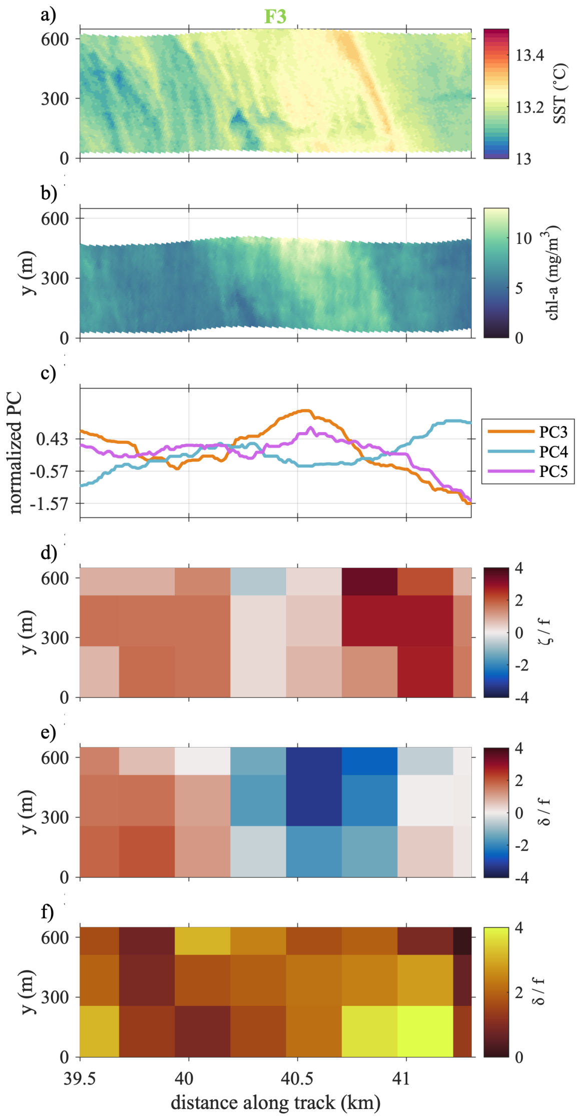

Figure 10. SST, chl-a, PCs 3-5, vorticity, divergence, and strain as in Fig. 8 for F3.

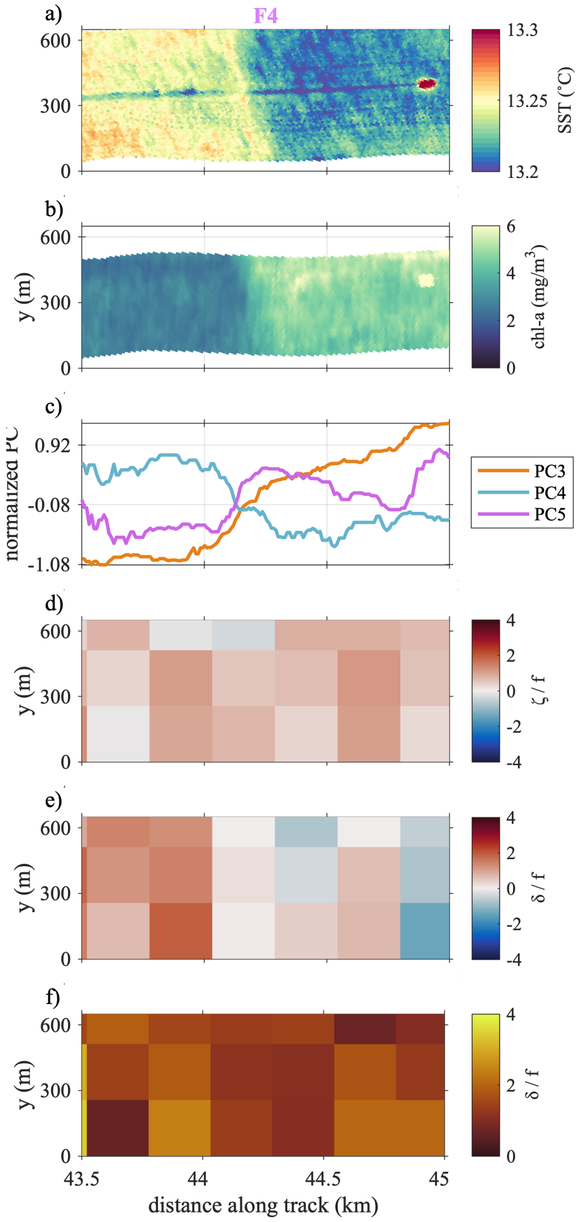

Figure 11. SST, chl-a, PCs 3-5, vorticity, divergence, and strain as in Fig. 8 for F4.

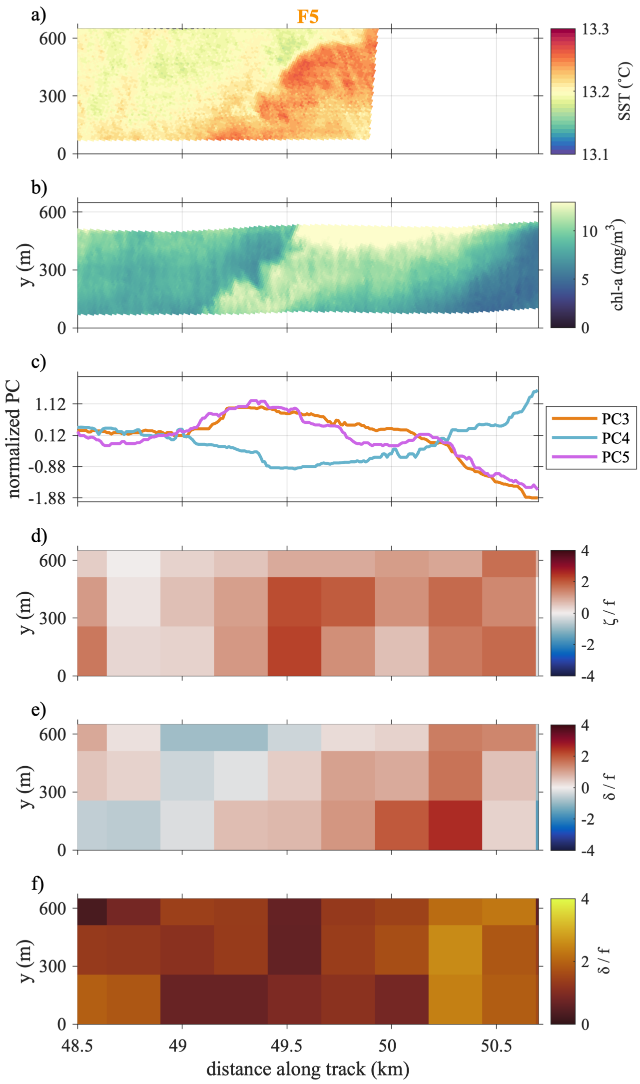

Figure 12. SST, chl-a, PCs 3-5, vorticity, divergence, and strain as in Fig. 8 for F5.

7. Summary and discussion

This study highlights the potential for suborbital remote sensing to quantify the impact of submesoscale processes on phytoplankton ecosystems and carbon transport. Merging bio-optical and physical airborne remote sensing data from the same platform avoids the spatiotemporal aliasing impacting in situ sensors and co-located remote sensing observations from different platforms. Here, we proposed a method to derive calibrated chlorophyll-a and particulate organic carbon from low altitude ocean color data, without the need for computationally-expensive atmospheric correction schemes. We merge concurrent airborne snapshots of sub-kilometer ocean velocities and their derivatives (i.e. vorticity, divergence, and strain), ocean color, and sea surface temperature to illuminate the influences of submesoscale dynamics on phytoplankton. This study works towards the detection and quantification of submesoscale bio-physical mechanisms using remote sensing. This could lead to the better understanding of the impacts of submesoscale dynamics on ocean biogeochemistry and their contributions to the ocean's role in climate.

Co-located, high resolution currents and hyperspectral ocean color can illuminate submesoscale bio-physical mechanisms that structure oceanic ecosystems and contribute to the vertical transport of carbon. Current derivatives at F1 (Fig. 8d-f) indicated active submesoscale frontogenesis, which is associated with an ageostrophic secondary circulation in the vertical which upwells water on the light side of the front and downwells water on the dense side of the front (Mahadevan 2016; Fig. 1e). The decrease of PC4 on the warm side of the front, in a region of enhanced convergence, may indicate the downwelling of a phytoplankton group undetected by chl-a. For example, picoplankton, such as prochlorococcus and synechococcus, are abundant in low chl-a waters. Changes in their concentrations may be detected by accessory pigment changes even if not detected in bulk chl-a measurements. Furthermore, phytoplankton community shifts may not be detected if there are concurrent increases and decreases in different phytoplankton groups that yield a near net zero change in chl-a.

F2 is not associated with a coherent dynamical signature (Fig. 9d-f), so its overall distribution is likely explained by stirring of warm water with high phytoplankton associated with PC3 (Fig. 1f). F2 also exhibits meter-scale, 'finger-like' features marked by warm, high chl-a waters (Fig. 9g). This 'quasi-periodic' SST variability may be due to the modulation of the diurnal warm layer's depth by internal waves when wind speeds are low and a diurnal warm layer is present (Farrar et al., 2007; Walsh et al., 1998). F4 confirms the presence of a diurnal warm layer 20 km down track (Fig. 11c) and wind speeds were around 4-6 m/s (Supporting Information Fig. S3). Patterns of phytoplankton may be driven by its accumulation in internal wave-driven convergence zones (Omand et al., 2011; Lenain & Pizzo 2021).

F3 could be associated with mechanisms depicted in Fig. 1c or Fig. 1e. Decreases in PC4 could be due to the downwelling of its associated phytoplankton, and increases in PC3 and PC5 could be due to the convergence and accumulation of its associated phytoplankton. In situ phytoplankton pigment or community data is needed to connect PC's with phytoplankton community groups to determine if PC3 and PC5 are associated with phytoplankton with depth-keeping behavior. Lastly, F5 is a region of high chl-a in a region of divergence and likely upwelling (Fig. 12a,e), possibly reflecting the impacts of mechanisms depicted in Fig. 1a or Fig. 1b.

The impacts of submesoscale dynamics and their vertical velocities on phytoplankton depend on the underlying vertical nutrient and chl-a structures, the depth that vertical velocities penetrate, and the limiting growth factor of phytoplankton (Mahadevan 2016). Hence, more work is needed to connect the surface to the underlying vertical velocity, nutrient, and chlorophyll-a structures. Observationally, this can be accomplished by using vertical profilers on ships and autonomous platforms integrating an Acoustic Doppler Current Profiler (ADCP), chlorophyll-a fluorometer to estimate phytoplankton concentrations, backscatter meter to estimate particle load and POC, and a sensor to estimate nitrate concentrations, the limiting macronutrient in the CCS. Process models will also be useful for describing the physics underlying remote sensing distributions and characterizing the evolution of the horizontal and vertical fields.

Ascribing mechanisms to relationships observed between hyperspectral ocean color, SST, and surface currents will require a synthesis of numerical and observational methods including process modeling and expanding the spatiotemporal scope of MASS data collection. This could lead to the detection of mechanisms, such as those depicted in Fig. 1, with a degree of statistical certainty. Refining ocean color corrections to increase confidence in airborne phytoplankton estimates will be a crucial next step in expanding the scope of MASS data.

Overall, removing sun glint and developing a more robust cloud mask for MASS will improve the ability to ascribe surface biology changes to submesoscale processes. This will provide stronger confidence that MASS is capturing real chl-a features without the need for reciprocal overpasses or ship overlaps. The best way to avoid sun glint is during data collection, such as by flying away from the glint on the sea surface (Mustard et al., 2001; Wang and Bailey 2001), avoiding windy conditions (Gordon and Wang 1992, 1994), and flying when the solar zenith angle is between 40-55° (Mustard et al., 2001), but these procedures are not always optimal for the remote sensing of currents. A post hoc sun glint correction and filtering of flights with optimal ocean color and physical data, as was done in this study, is most suitable for this type of dataset. A more sophisticated glint correction than the black pixel assumption could improve agreement between repeat overpasses and ship data.

Changing viewing and solar geometries between overpasses also presents a challenge for airborne remote sensing. Here, we partially account for changing geometries using statistical methods to predict chl-a and POC from all available flights that made parallel overlaps with the ship track. However, our chl-a and POC models were created for a limited spatiotemporal range with a finite set of viewing and solar geometries. Any subsequent studies should attempt a calibration and in situ evaluation similar to the methods described in Section 4. Additionally, more work is needed to test if the model can be applied outside of training conditions. Expanding the training data to include a larger dynamic range and more solar and viewing geometries could help strengthen the predictive power of the models (Lang et al., 2023c). The models, when applied to the full swath, were better at capturing relative changes in chl-a and POC than their magnitudes (Fig. 5). When the model (developed with across-track median $r_{rs}(\lambda)$) was applied to every pixel across the full swath, sun glint likely became more significant and raised the values of chl-a and POC plotted in Fig.5. The models also have larger errors at high chl-a values as shown in Fig. 4.

Hyperspectral measurements can yield products beyond chl-a and POC. Principal component analysis applied to the full hyperspectral data decomposed the data into spectral signatures associated with water and its optical constituents. For example, PC1 captured the variability in-water absorption and particulate backscattering, PC2 captured the variability in chl-a, and higher PC's captured small peaks likely associated with phytoplankton pigments. This suggests that applying pigment based algorithms, which rely on the ability to resolve narrow spectral features related to accessory pigments (Kramer et al., 2022), will be successful when applied to MASS data. In situ validation data, such as pigments analyzed with High Performance Liquid Chromatography or phytoplankton assemblages identified with flow cytometry, can be used to tune algorithms predicting phytoplankton community groups (Kramer et al., 2022; Lange et al., 2020). Future studies combining MASS currents and SST with phytoplankton community distributions could disentangle the impact of submesoscale dynamics on phytoplankton community groups.

Open Research Section

Presented data and code to generate figures were archived with the UC San Diego Library Digital Collections (`https://doi.org/10.6075/J0RN386Z`). Data in this paper was collected during the Submesoscale Ocean Dynamics Experiment (S-MODE). The S-MODE data presented in this manuscript is publicly available via the Physical Oceanography Distributed Active Archive Center (PO.DAAC) at https://podaac.jpl.nasa.gov/S-MODE. Hyperspectral data from the Modular Aerial Sensing System (MASS) can be downloaded here: https://doi.org/10.5067/SMODE-MASS1H. MASS long wave infrared imagery (LWIR) can be downloaded here: https://doi.org/10.5067/SMODE-MASS1I. MASS DoppVis imagery can be downloaded here: https://doi.org/10.5067/SMODE-MASS1D. Shipboard bottle data can be downloaded here: https://doi.org/10.5067/SMODE-RVBOT. Shipboard flow-through data can be downloaded here: https://doi.org/10.5067/SMODE-RVTSG. Sentinel-3 OLCI Level-2 (Full Resolution) and Sentinel-3 SLSTR Level-2 Sea Surface Temperature (SST) data can be downloaded from the EUMETSAT User Portal here: https://data.eumetsat.int/. Data presented in Fig. 2 was captured on October 29, 2021 in the following bounding box: [36.1, -126], [36.1, -121], [38.3, -126], [38.3, -121].

Acknowledgments

This work was supported by NASA awards to M. Omand 80NSSC19K1037 and L. Lenain 80NSSC19K1688, with student support for S. Lang from the NASA Rhode Island Space Grant Consortium (AWD11155). We thank the entire S-MODE science team for data collection, discussion, and feedback. We thank Roger 'Pat' Kelly for his all work on in situ sample collection and processing. We thank Mara Freilich for her feedback, scientific discussions, and code for kinetic energy flux calculations. We thank the crew of the R/V Oceanus and the MASS team from the Air Sea Interactions Laboratory at the Scripps Institution of Oceanography, especially Nick Statom. Statom and Stephen Deaton both provided MATLAB codes for reading in raw airborne data. Inés Leyba helped conduct an analysis of wind conditions using 3-km High-Resolution Rapid Refresh product and Wave Gliders to assist in the investigation of features shown in Fig. 9g.

References

Aluie, H., Hecht, M., & Vallis, G. K. (2018, February). Mapping the Energy Cascade in the North Atlantic Ocean: The Coarse-Graining Approach. *Journal of Physical Oceanography*, *48*(2), 225–244. Retrieved from `https://journals.ametsoc.org/view/journals/phoc/48/2/jpo-d-17-0100.1.xml` (https://doi.org/10.1175/JPO-D-17-0100.1) doi: https://doi.org/10.1175/JPO-D-17-0100.1

Amos, C. M., Castelao, R. M., & Medeiros, P. M. (2019, October). Offshore transport of particulate organic carbon in the California Current System by mesoscale eddies. *Nature Communications*, *10*(1), 4940. Retrieved from `https://doi.org/10.1038/s41467-019-12783-5` (https://doi.org/10.1038/s41467-019-12783-5) doi: 10.1038/s41467-019-12783-5

Baith, K., Lindsay, R., Fu, G., & McClain, C. R. (2001). Data analysis system developed for ocean color satellite sensors. *Eos, Transactions American Geophysical Union*, *82*(18), 202–202. Retrieved 2024-12-10, from `https://onlinelibrary.wiley.com/doi/abs/10.1029/01EO00109` (https://doi.org/10.1029/01EO00109) doi: 10.1029/01EO00109

Balwada, D., Xiao, Q., Smith, S., Abernathey, R., & Gray, A. R. (2021, September). Vertical Fluxes Conditioned on Vorticity and Strain Reveal Submesoscale Ventilation. *Journal of Physical Oceanography*, *51*(9), 2883–2901. Retrieved from `https://journals.ametsoc.org/view/journals/phoc/51/`

9/JPO-D-21-0016.1.xml (https://doi.org/10.1175/JPO-D-21-0016.1) doi: 10.1175/JPO-D-21-0016.1

Balwada, D., Xie, J.-H., Marino, R., & Feraco, F. (2022, October). Direct observational evidence of an oceanic dual kinetic energy cascade and its seasonality. *Science Advances*, *8*(41), eabq2566. Retrieved 2023-12-19, from https://doi.org/10.1126/sciadv.abq2566 (https://doi.org/10.1126/sciadv.abq2566) doi: 10.1126/sciadv.abq2566

Barkan, R., Molemaker, M. J., Srinivasan, K., McWilliams, J. C., & D'Asaro, E. A. (2019, June). The Role of Horizontal Divergence in Submesoscale Frontogenesis. *Journal of Physical Oceanography*, *49*(6), 1593–1618. Retrieved from https://journals.ametsoc.org/view/journals/phoc/49/6/jpo-d-18-0162.1.xml (https://doi.org/10.1175/JPO-D-18-0162.1) doi: 10.1175/JPO-D-18-0162.1

Boccaletti, G., Ferrari, R., & Fox-Kemper, B. (2007, September). Mixed Layer Instabilities and Restratification. *Journal of Physical Oceanography*, *37*(9), 2228–2250. Retrieved from https://journals.ametsoc.org/view/journals/phoc/37/9/jpo3101.1.xml (https://doi.org/10.1175/JPO3101.1) doi: 10.1175/JPO3101.1

Bracher, A., Taylor, M. H., Taylor, B., Dinter, T., Röttgers, R., & Steinmetz, F. (2015, February). Using empirical orthogonal functions derived from remote-sensing reflectance for the prediction of phytoplankton pigment concentrations. *Ocean Science*, *11*(1), 139–158. Retrieved 2024-05-20, from https://os.copernicus.org/articles/11/139/2015/ (https://doi.org/10.5194/os-11-139-2015) doi: 10.5194/os-11-139-2015

Checkley, D. M., & Barth, J. A. (2009, December). Patterns and processes in the California Current System. *Progress in Oceanography*, *83*(1), 49–64. Retrieved from https://www.sciencedirect.com/science/article/pii/S0079661109001098 (https://doi.org/10.1016/j.pocean.2009.07.028) doi: 10.1016/j.pocean.2009.07.028

Craig, S. E., Jones, C. T., Li, W. K. W., Lazin, G., Horne, E., Caverhill, C., & Cullen, J. J. (2012, April). Deriving optical metrics of coastal phytoplankton biomass from ocean colour. *Remote Sensing of Environment*, *119*, 72–83. Retrieved 2024-05-20, from https://www.sciencedirect.com/science/article/pii/S0034425711004445 (https://doi.org/10.1016/j.rse.2011.12.007) doi: 10.1016/j.rse.2011.12.007

D'Asaro, E., Lee, C., Rainville, L., Harcourt, R., & Thomas, L. (2011, April). Enhanced Turbulence and Energy Dissipation at Ocean Fronts. *Science*, *332*(6027), 318–322. Retrieved 2024-12-10, from https://www.science.org/doi/10.1126/science.1201515 (https://doi.org/10.1126/science.1201515) doi: 10.1126/science.1201515

Eyink, G. L. (2005, July). Locality of turbulent cascades. *Physica D: Nonlinear Phenomena*, *207*(1), 91–116. Retrieved 2024-06-20, from https://www.sciencedirect.com/science/article/pii/S0167278905002253 (https://doi.org/10.1016/j.physd.2005.05.018) doi: 10.1016/j.physd.2005.05.018

Farrar, J. T., D'Asaro, E., Rodriguez, E., Shcherbina, A., Czech, E., Matthias, P., ... Jenkins, R. (2020, October). S-MODE: The Sub-Mesoscale Ocean Dynamics Experiment. In *IGARSS 2020 - 2020 IEEE International Geoscience and Remote Sensing Symposium* (pp. 3533–3536). (https://doi.org/10.1109/IGARSS39084.2020.9323112) doi: 10.1109/IGARSS39084.2020.9323112

Farrar, J. T., Zappa, C. J., Weller, R. A., & Jessup, A. T. (2007). Sea surface temperature signatures of oceanic internal waves in low winds. *Journal of Geophysical Research: Oceans*, *112*(C6). Retrieved 2024-11-20, from https://onlinelibrary.wiley.com/doi/abs/10.1029/2006JC003947 (https://doi.org/10.1029/2006JC003947) doi: 10.1029/2006JC003947

Ferrari, R., & Wunsch, C. (2009, January). Ocean Circulation Kinetic Energy: Reservoirs, Sources, and Sinks. *Annual Review of Fluid Mechanics*, *41*(Volume 41, 2009), 253–282. Retrieved 2024-06-25, from `https://www.annualreviews.org/content/journals/10.1146/annurev.fluid.40.111406.102139` (https://doi.org/10.1146/annurev.fluid.40.111406.102139) doi: 10.1146/annurev.fluid.40.111406.102139

Fox-Kemper, B., & Ferrari, R. (2008, June). Parameterization of Mixed Layer Eddies. Part II: Prognosis and Impact. *Journal of Physical Oceanography*, *38*(6), 1166–1179. Retrieved from `https://journals.ametsoc.org/view/journals/phoc/38/6/2007jpo3788.1.xml` (https://doi.org/10.1175/2007JPO3788.1) doi: 10.1175/2007JPO3788.1

Freilich, M., Lenain, L., & Gille, S. T. (2023). Characterizing the Role of Non-Linear Interactions in the Transition to Submesoscale Dynamics at a Dense Filament. *Geophysical Research Letters*, *50*(15), e2023GL103745. Retrieved 2024-06-06, from `https://onlinelibrary.wiley.com/doi/abs/10.1029/2023GL103745` (https://doi.org/10.1029/2023GL103745) doi: 10.1029/2023GL103745

Freilich, M. A., Poirier, C., Dever, M., Alou-Font, E., Allen, J., Cabornero, A., . . . Mahadevan, A. (2024, May). 3D intrusions transport active surface microbial assemblages to the dark ocean. *Proceedings of the National Academy of Sciences*, *121*(19), e2319937121. Retrieved 2024-11-20, from `https://www.pnas.org/doi/abs/10.1073/pnas.2319937121` (https://doi.org/10.1073/pnas.2319937121) doi: 10.1073/pnas.2319937121

Fu, L.-L., Pavelsky, T., Cretaux, J.-F., Morrow, R., Farrar, J. T., Vaze, P., . . . Dibarboure, G. (2024). The surface water and ocean topography mission: A breakthrough in radar remote sensing of the ocean and land surface water. *Geophysical Research Letters*, *51*(4), e2023GL107652. Retrieved from `https://agupubs.onlinelibrary.wiley.com/doi/abs/10.1029/2023GL107652` (https://doi.org/10.1029/2023GL107652) doi: https://doi.org/10.1029/2023GL107652

García-Reyes, M., & Largier, J. L. (2012, March). Seasonality of coastal upwelling off central and northern California: New insights, including temporal and spatial variability. *Journal of Geophysical Research: Oceans*, *117*(C3). Retrieved 2024-07-08, from `https://doi.org/10.1029/2011JC007629` (https://doi.org/10.1029/2011JC007629) doi: 10.1029/2011JC007629

Germano, M. (1992, May). Turbulence: the filtering approach. *Journal of Fluid Mechanics*, *238*, 325–336. Retrieved 2024-06-20, from `https://www.cambridge.org/core/journals/journal-of-fluid-mechanics/article/abs/turbulence-the-filtering-approach/1B92D8CFAEEB0D6B4ADA6BB31282D378` (https://doi.org/10.1017/S0022112092001733) doi: 10.1017/S0022112092001733

Gordon, H. R., & Wang, M. (1992, July). Surface-roughness considerations for atmospheric correction of ocean color sensors. 1: The Rayleigh-scattering component. *Applied Optics*, *31*(21), 4247–4260. Retrieved 2024-06-27, from `https://opg.optica.org/ao/abstract.cfm?uri=ao-31-21-4247` (https://doi.org/10.1364/AO.31.004247) doi: 10.1364/AO.31.004247

Gordon, H. R., & Wang, M. (1994, January). Retrieval of water-leaving radiance and aerosol optical thickness over the oceans with SeaWiFS: a preliminary algorithm. *Applied Optics*, *33*(3), 443–452. Retrieved 2024-06-27, from `https://opg.optica.org/ao/abstract.cfm?uri=ao-33-3-443` (https://doi.org/10.1364/AO.33.000443) doi: 10.1364/AO.33.000443

Homolova, L., Alanko-Huotari, K., & Scheapman, M. E. (2009, August). Sensitivity of the ground-based downwelling irradiance recorded by the FODIS sensor in respect of different angular positions. In *2009 First Workshop on Hyperspectral Image and Signal Processing: Evolution in Remote Sensing* (pp. 1–4). (https://doi.org/10.1109/WHISPERS.2009.5289084) doi: 10.1109/WHISPERS.2009.5289084

Jones-Kellett, A. E., & Follows, M. J. (2024, March). A Lagrangian coherent eddy atlas for biogeochemical applications in the North Pacific Subtropical Gyre. *Earth System Science Data*, *16*(3), 1475–1501. Retrieved 2024-11-20, from `https://essd.copernicus.org/articles/16/1475/2024/` (https://doi.org/10.5194/essd-16-1475-2024) doi: 10.5194/essd-16-1475-2024

Kang, X., Gao, G., Hao, Q., & Li, S. (2019). A coarse-to-fine method for cloud detection in remote sensing images. *IEEE Geoscience and Remote Sensing Letters*, *16*(1), 110-114. (https://doi.org/10.1109/LGRS.2018.2866499) doi: 10.1109/LGRS.2018.2866499

Kramer, S. J., Siegel, D. A., Maritorena, S., & Catlett, D. (2022, March). Modeling surface ocean phytoplankton pigments from hyperspectral remote sensing reflectance on global scales. *Remote Sensing of Environment*, *270*, 112879. Retrieved 2024-06-28, from `https://www.sciencedirect.com/science/article/pii/S003442572100599X` (https://doi.org/10.1016/j.rse.2021.112879) doi: 10.1016/j.rse.2021.112879

Lang, S. E., Kelly, R. P., & Omand, M. M. (2023). *S-MODE Shipboard Flow-through Bio-Optical Measurements Version 1. Ver. 1.* CA, USA: PO.DAAC. (https://doi.org/10.5067/SMODE-RVBO2) doi: https://doi.org/10.5067/SMODE-RVBO2

Lang, S. E., Kelly, R. P., Outram, D. M., Thomas, C. S., & Omand, M. (2022). *S-MODE Shipboard Bottle Data Version 1. Ver. 1.* CA, USA: PO.DAAC. (https://doi.org/10.5067/SMODE-RVBOT) doi: https://doi.org/10.5067/SMODE-RVBOT

Lang, S. E., Luis, K. M. A., Doney, S. C., Cronin-Golomb, O., & Castorani, M. C. N. (2023, July). Modeling Coastal Water Clarity Using Landsat-8 and Sentinel-2. *Earth and Space Science*, *10*(7), e2022EA002579. Retrieved 2024-07-08, from `https://doi.org/10.1029/2022EA002579` (https://doi.org/10.1029/2022EA002579) doi: 10.1029/2022EA002579

Lange, P. K., Werdell, P. J., Erickson, Z. K., Dall'Olmo, G., Brewin, R. J. W., Zubkov, M. V., … Cetinić, I. (2020, August). Radiometric approach for the detection of picophytoplankton assemblages across oceanic fronts. *Optics Express*, *28*(18), 25682–25705. Retrieved 2024-05-20, from `https://opg.optica.org/oe/abstract.cfm?uri=oe-28-18-25682` (https://doi.org/10.1364/OE.398127) doi: 10.1364/OE.398127

Lenain, L., & Melville, W. K. (2017, August). Measurements of the Directional Spectrum across the Equilibrium Saturation Ranges of Wind-Generated Surface Waves. *Journal of Physical Oceanography*, *47*(8), 2123–2138. Retrieved from `https://journals.ametsoc.org/view/journals/phoc/47/8/jpo-d-17-0017.1.xml` (https://doi.org/10.1175/JPO-D-17-0017.1) doi: 10.1175/JPO-D-17-0017.1

Lenain, L., & Pizzo, N. (2020, December). The Contribution of High-Frequency Wind-Generated Surface Waves to the Stokes Drift. *Journal of Physical Oceanography*, *50*(12), 3455–3465. Retrieved 2024-06-28, from `https://journals.ametsoc.org/view/journals/phoc/50/12/JPO-D-20-0116.1.xml` (https://doi.org/10.1175/JPO-D-20-0116.1) doi: 10.1175/JPO-D-20-0116.1

Lenain, L., & Pizzo, N. (2021, September). Modulation of Surface Gravity Waves by Internal Waves. Retrieved 2024-06-28, from `https://journals.ametsoc.org/view/journals/phoc/51/9/JPO-D-20-0302.1.xml` (https://doi.org/10.1175/JPO-D-20-0302.1) doi: 10.1175/JPO-D-20-0302.1

Lenain, L., Smeltzer, B. K., Pizzo, N., Freilich, M., Colosi, L., Ellingsen, S. , … Statom, N. (2023, April). Airborne Remote Sensing of Upper-Ocean and Surface Properties, Currents and Their Gradients From Meso to Submesoscales. *Geophysical Research Letters*, *50*(8), e2022GL102468. Retrieved 2023-11-29, from `https://doi.org/10.1029/2022GL102468` (https://doi.org/10.1029/2022GL102468) doi: 10.1029/2022GL102468

Lenain, L., Statom, N. M., & Melville, W. K. (2019, November). Airborne Measurements of Surface Wind and Slope Statistics over the Ocean. *Journal of Physical Oceanography*, *49*(11), 2799–2814. Retrieved from https://journals.ametsoc.org/view/journals/phoc/49/11/jpo-d-19-0098.1.xml (https://doi.org/10.1175/JPO-D-19-0098.1) doi: 10.1175/JPO-D-19-0098.1

Lévy, M., Couespel, D., Haëck, C., Keerthi, M. G., Mangolte, I., & Prend, C. J. (2024, January). The Impact of Fine-Scale Currents on Biogeochemical Cycles in a Changing Ocean. *Annual Review of Marine Science*, *16*(Volume 16, 2024), 191–215. Retrieved 2024-11-20, from https://www.annualreviews.org/content/journals/10.1146/annurev-marine-020723-020531 (https://doi.org/10.1146/annurev-marine-020723-020531) doi: 10.1146/annurev-marine-020723-020531

Lévy, M., Franks, P. J. S., & Smith, K. S. (2018, November). The role of submesoscale currents in structuring marine ecosystems. *Nature Communications*, *9*(1), 4758. Retrieved from https://doi.org/10.1038/s41467-018-07059-3 (https://doi.org/10.1038/s41467-018-07059-3) doi: 10.1038/s41467-018-07059-3

Lévy, M., Jahn, O., Dutkiewicz, S., Follows, M. J., & d'Ovidio, F. (2015, October). The dynamical landscape of marine phytoplankton diversity. *Journal of The Royal Society Interface*, *12*(111), 20150481. Retrieved 2024-06-28, from https://royalsocietypublishing.org/doi/full/10.1098/rsif.2015.0481 (https://doi.org/10.1098/rsif.2015.0481) doi: 10.1098/rsif.2015.0481

Mahadevan, A. (2016, January). The Impact of Submesoscale Physics on Primary Productivity of Plankton. *Annual Review of Marine Science*, *8*(1), 161–184. Retrieved 2023-12-19, from https://doi.org/10.1146/annurev-marine-010814-015912 (https://doi.org/10.1146/annurev-marine-010814-015912) doi: 10.1146/annurev-marine-010814-015912

Mahadevan, A., & Tandon, A. (2006, January). An analysis of mechanisms for submesoscale vertical motion at ocean fronts. *Ocean Modelling*, *14*(3), 241–256. Retrieved 2024-01-04, from https://www.sciencedirect.com/science/article/pii/S1463500306000540 (https://doi.org/10.1016/j.ocemod.2006.05.006) doi: 10.1016/j.ocemod.2006.05.006

Mauzole, Y. L., Torres, H. S., & Fu, L.-L. (2020, February). Patterns and Dynamics of SST Fronts in the California Current System. *Journal of Geophysical Research: Oceans*, *125*(2), e2019JC015499. Retrieved 2024-07-08, from https://doi.org/10.1029/2019JC015499 (https://doi.org/10.1029/2019JC015499) doi: 10.1029/2019JC015499

McWilliams, J. C. (2016, May). Submesoscale currents in the ocean. *Proceedings. Mathematical, Physical, and Engineering Sciences / The Royal Society*, *472*(2189), 20160117. Retrieved 2024-06-26, from https://www.ncbi.nlm.nih.gov/pmc/articles/PMC4893189/ (https://doi.org/10.1098/rspa.2016.0117) doi: 10.1098/rspa.2016.0117

McWilliams, J. C., Colas, F., & Molemaker, M. J. (2009). Cold filamentary intensification and oceanic surface convergence lines. *Geophysical Research Letters*, *36*(18). Retrieved 2024-11-20, from https://doi.org/110.1029/2009GL039402 (_eprint: https://onlinelibrary.wiley.com/doi/pdf/10.1029/2009GL039402) doi: 10.1029/2009GL039402

Melville, W. K., Lenain, L., Cayan, D. R., Kahru, M., Kleissl, J. P., Linden, P. F., & Statom, N. M. (2016, June). The Modular Aerial Sensing System. *Journal of Atmospheric and Oceanic Technology*, *33*(6), 1169–1184. Retrieved from https://journals.ametsoc.org/view/journals/atot/33/6/jtech-d-15-0067_1.xml (https://doi.org/10.1175/JTECH-D-15-0067.1) doi: 10.1175/JTECH-D-15-0067.1

Mikofski, M. (2024, June). *Solar Position Calculator.* Retrieved 2024-06-28, from https://www.mathworks.com/matlabcentral/fileexchange/58405-solar-position-calculator (https://www.mathworks.com/matlabcentral/fileexchange/58405-solar-position-

calculator)
Mobley, C. D., Werdell, J., Franz, B., Ahmad, Z., & Bailey, S. (2016, June). Atmospheric Correction for Satellite Ocean Color Radiometry. (https://doi.org/10.13140/RG.2.2.23016.78081)
Mustard, J. F., Staid, M. I., & Fripp, W. J. (2001, March). A Semianalytical Approach to the Calibration of AVIRIS Data to Reflectance over Water: Application in a Temperate Estuary. *Remote Sensing of Environment*, *75*(3), 335–349. Retrieved 2024-06-28, from https://www.sciencedirect.com/science/article/pii/S0034425700001772 (https://doi.org/10.1016/S0034-4257(00)00177-2) doi: 10.1016/S0034-4257(00)00177-2
Omand, M. M., D'Asaro, E. A., Lee, C. M., Perry, M. J., Briggs, N., Cetinić, I., & Mahadevan, A. (2015, April). Eddy-driven subduction exports particulate organic carbon from the spring bloom. *Science*, *348*(6231), 222–225. Retrieved 2024-06-28, from https://www.science.org/doi/10.1126/science.1260062 (https://doi.org/10.1126/science.1260062) doi: 10.1126/science.1260062
Omand, M. M., Leichter, J. J., Franks, P. J. S., Guza, R. T., Lucas, A. J., & Feddersen, F. (2011). Physical and biological processes underlying the sudden surface appearance of a red tide in the nearshore. *Limnology and Oceanography*, *56*(3), 787–801. Retrieved 2024-11-20, from https://onlinelibrary.wiley.com/doi/abs/10.4319/lo.2011.56.3.0787 (https://doi.org/10.4319/lo.2011.56.3.0787) doi: 10.4319/lo.2011.56.3.0787
O'Reilly, J. E., Maritorena, S., Mitchell, B. G., Siegel, D. A., Carder, K. L., Garver, S. A., ... McClain, C. (1998, October). Ocean color chlorophyll algorithms for SeaWiFS. *Journal of Geophysical Research: Oceans*, *103*(C11), 24937–24953. Retrieved 2024-07-08, from https://doi.org/10.1029/98JC02160 (https://doi.org/10.1029/98JC02160) doi: 10.1029/98JC02160
O'Reilly, J. E., & Werdell, P. J. (2019, August). Chlorophyll algorithms for ocean color sensors - OC4, OC5 & OC6. *Remote Sensing of Environment*, *229*, 32–47. Retrieved 2024-06-28, from https://www.sciencedirect.com/science/article/pii/S003442571930166X (https://doi.org/10.1016/j.rse.2019.04.021) doi: 10.1016/j.rse.2019.04.021
Pereira, F., da Silveira, I. C. A., Tandon, A., Franks, P. J. S., Luko, C. D., Santos, D. M. C., ... Brandini, F. P. (2024). Phytoplankton Responses to Mesoscale and Submesoscale Processes in a Tropical Meander. *Journal of Geophysical Research: Oceans*, *129*(6), e2023JC020685. Retrieved 2024-11-20, from https://onlinelibrary.wiley.com/doi/abs/10.1029/2023JC020685 (https://doi.org//10.1029/2023JC020685) doi: 10.1029/2023JC020685
Plummer, A., Freilich, M., Benzi, R., Choi, C. J., Sudek, L., Worden, A. Z., ... Mahadevan, A. (2023). Oceanic Frontal Divergence Alters Phytoplankton Competition and Distribution. *Journal of Geophysical Research: Oceans*, *128*(8), e2023JC019902. Retrieved 2024-11-20, from https://onlinelibrary.wiley.com/doi/abs/10.1029/2023JC019902 (https://doi.org/10.1029/2023JC019902) doi: 10.1029/2023JC019902
Sathyendranath, S., Hoge, F. E., Platt, T., & Swift, R. N. (1994, February). Detection of phytoplankton pigments from ocean color: improved algorithms. *Applied Optics*, *33*(6), 1081–1089. Retrieved 2024-11-20, from https://opg.optica.org/ao/abstract.cfm?uri=ao-33-6-1081 (https://doi.org/10.1364/AO.33.001081) doi: 10.1364/AO.33.001081
Siegel, D. A., DeVries, T., Cetinić, I., & Bisson, K. M. (2023, January). Quantifying the Ocean's Biological Pump and Its Carbon Cycle Impacts on Global Scales. *Annual Review of Marine Science*, *15*(Volume 15, 2023), 329–356. Retrieved 2024-11-20, from https://www.annualreviews.org/content/journals/10.1146/annurev-marine-040722-115226 (https://doi.org/10.1146/annurev-marine-040722-115226) doi: 10.1146/annurev-marine-040722-115226

Srinivasan, K., Barkan, R., & McWilliams, J. C. (2023, January). A Forward Energy Flux at Submesoscales Driven by Frontogenesis. *Journal of Physical Oceanography*, *53*(1), 287–305. Retrieved from https://journals.ametsoc.org/view/journals/phoc/53/1/JPO-D-22-0001.1.xml (https://doi.org/10.1175/JPO-D-22-0001.1) doi: 10.1175/JPO-D-22-0001.1

Steinmetz, F., Deschamps, P.-Y., & Ramon, D. (2011, May). Atmospheric correction in presence of sun glint: application to MERIS. *Optics Express*, *19*(10), 9783–9800. Retrieved 2024-12-10, from https://opg.optica.org/oe/abstract.cfm?uri=oe-19-10-9783 (https://doi.org/10.1364/OE.19.009783) doi: 10.1364/OE.19.009783

Stramski, D., Reynolds, R. A., Babin, M., Kaczmarek, S., Lewis, M. R., Röttgers, R., . . . Claustre, H. (2008, February). Relationships between the surface concentration of particulate organic carbon and optical properties in the eastern South Pacific and eastern Atlantic Oceans. *Biogeosciences*, *5*(1), 171–201. Retrieved 2024-06-28, from https://bg.copernicus.org/articles/5/171/2008/ (https://doi.org/10.5194/bg-5-171-2008) doi: 10.5194/bg-5-171-2008

Taylor, A. G., Goericke, R., Landry, M. R., Selph, K. E., Wick, D. A., & Roadman, M. J. (2012, September). Sharp gradients in phytoplankton community structure across a frontal zone in the California Current Ecosystem. *Journal of Plankton Research*, *34*(9), 778–789. Retrieved 2024-06-28, from https://doi.org/10.1093/plankt/fbs036 (https://doi.org/10.1093/plankt/fbs036) doi: 10.1093/plankt/fbs036

Taylor, J. R. (2018, June). Accumulation and Subduction of Buoyant Material at Submesoscale Fronts. *Journal of Physical Oceanography*, 1233–1241. Retrieved 2024-11-20, from https://journals.ametsoc.org/view/journals/phoc/48/6/jpo-d-17-0269.1.xml (https://doi.org/10.1175/JPO-D-17-0269.1) doi: 10.1175/JPO-D-17-0269.1

Taylor, J. R., & Thompson, A. F. (2023, January). Submesoscale Dynamics in the Upper Ocean. *Annual Review of Fluid Mechanics*, *55*(1), 103–127. Retrieved 2023-12-19, from https://doi.org/10.1146/annurev-fluid-031422-095147 (https://doi.org/10.1146/annurev-fluid-031422-095147) doi: 10.1146/annurev-fluid-031422-095147

Thomas, L. N., Tandon, A., & Mahadevan, A. (2008, January). Submesoscale Processes and Dynamics. In *Ocean Modeling in an Eddying Regime* (pp. 17–38). Retrieved 2023-12-19, from https://doi.org/10.1029/177GM04 (https://doi.org/10.1029/177GM04)

Villas Bôas, A. B., Lenain, L., Cornuelle, B. D., Gille, S. T., & Mazloff, M. R. (2022). A Broadband View of the Sea Surface Height Wavenumber Spectrum. *Geophysical Research Letters*, *49*(4), e2021GL096699. Retrieved 2024-06-28, from https://onlinelibrary.wiley.com/doi/abs/10.1029/2021GL096699 (https://doi.org/10.1029/2021GL096699) doi: 10.1029/2021GL096699

Vishnu, P. S., Xi, H., Belluz, J. D. B., Hussain, M. S., Bracher, A., & Costa, M. (2022, November). Seasonal dynamics of major phytoplankton functional types in the coastal waters of the west coast of Canada derived from OLCI Sentinel 3A. *Frontiers in Marine Science*, *9*. Retrieved 2024-11-20, from https://www.frontiersin.org/journals/marine-science/articles/10.3389/fmars.2022.1018510/full (https://doi.org/10.3389/fmars.2022.1018510) doi: 10.3389/fmars.2022.1018510

Walsh, E. J., Pinkel, R., Hagan, D. E., Weller, R. A., Fairall, C. W., Rogers, D. P., . . . Baumgartner, M. (1998). Coupling of internal waves on the main thermocline to the diurnal surface layer and sea surface temperature during the Tropical Ocean-Global Atmosphere Coupled Ocean-Atmosphere Response Experiment. *Journal of Geophysical Research: Oceans*, *103*(C6), 12613–12628. Retrieved 2024-11-20, from https://onlinelibrary.wiley.com/doi/abs/10.1029/98JC00894 (https://doi.org/10.1029/98JC00894) doi: 10.1029/98JC00894

Wang, M., & Bailey, S. W. (2001, September). Correction of Sun glint Contamination on the SeaWiFS Ocean and Atmosphere Products. *Applied Optics*, *40*(27), 4790–4798. (https://doi.org/10.1364/ao.40.004790) doi: 10.1364/ao.40.004790

Zhang, Z., Qiu, B., Klein, P., & Travis, S. (2019, June). The influence of geostrophic strain on oceanic ageostrophic motion and surface chlorophyll. *Nature Communications*, *10*, 2838. Retrieved 2024-03-11, from https://www.ncbi.nlm.nih.gov/pmc/articles/PMC6599054/ (https://doi.org/10.1038/s41467-019-10883-w) doi: 10.1038/s41467-019-10883-w

Supporting Information for: Airborne remote sensing of concurrent submesoscale dynamics and phytoplankton

Sarah Lang[1], Melissa Omand[1], Luc Lenain[2]

[1] Graduate School of Oceanography, University of Rhode Island, Narragansett, RI 02882, USA

[2] Scripps Institution of Oceanography, La Jolla, CA 92037, USA

Contents of file:

- Table S1
- Table S2
- Figure S1
- Figure S2
- Figure S3

Introduction This file contains supplementary tables and figures referenced in the paper: Airborne remote sensing of concurrent submesoscale dynamics and phytoplankton. Contents support the findings presented in the paper. Tables S1 and S2 display regression results used to estimate chlorophyll-a and particulate organic carbon from the hyperspectral camera on the Modular Aerial Sensing System (MASS, SIO). Figures S1 and S2 support results from Section 5 of the paper and Figure S3 is referenced in Section 7 to support the interpretation of airborne data in the manuscript.

1 Table S1

Chl-a regression results

Variable	B	SE	t	p
(Intercept)	0.286	0.014	20.37	P<0.001
rrs486 / rrs555	-2.04	0.15	-14	P<0.001
pitch	0.06	0.0043	1.36	0.18
altitude	0	0	-1.06	0.29
sza (solar zenith angle)	0.018	0.0055	3.25	0.0017
rrs486 / rrs555 * altitude	-0.0031	0.00084	-3.70	P<0.001
pitch * altitude	-0.00037	0.00017	-2.25	0.027

2 Table S2

POC regression results

Variable	B	SE	t	p
(Intercept)	1.41	0.010	135.43	P<0.001
rrs486 / rrs555	-1.46	0.11	-12.76	P<0.001
altitude	0	0	0.31	0.76
sza (solar zenith angle)	0.025	0.0047	5.20	P<0.001
rrs486 / rrs555 * altitude	-0.0023	0.00065	-3.50	P<0.001

3 Figure S1

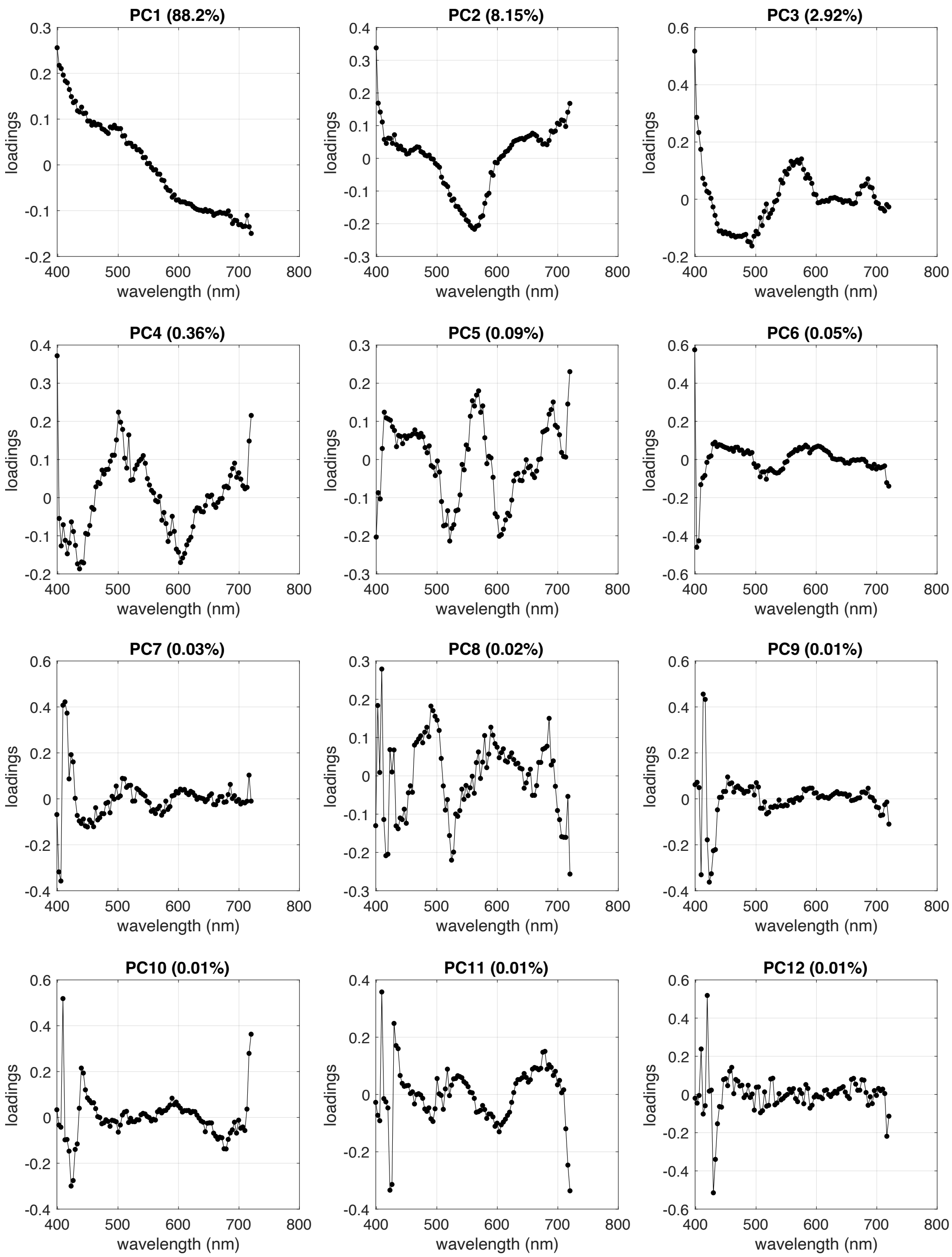

Figure 1: Loadings and percent variances for first 12 principal components.

4 Figure S2

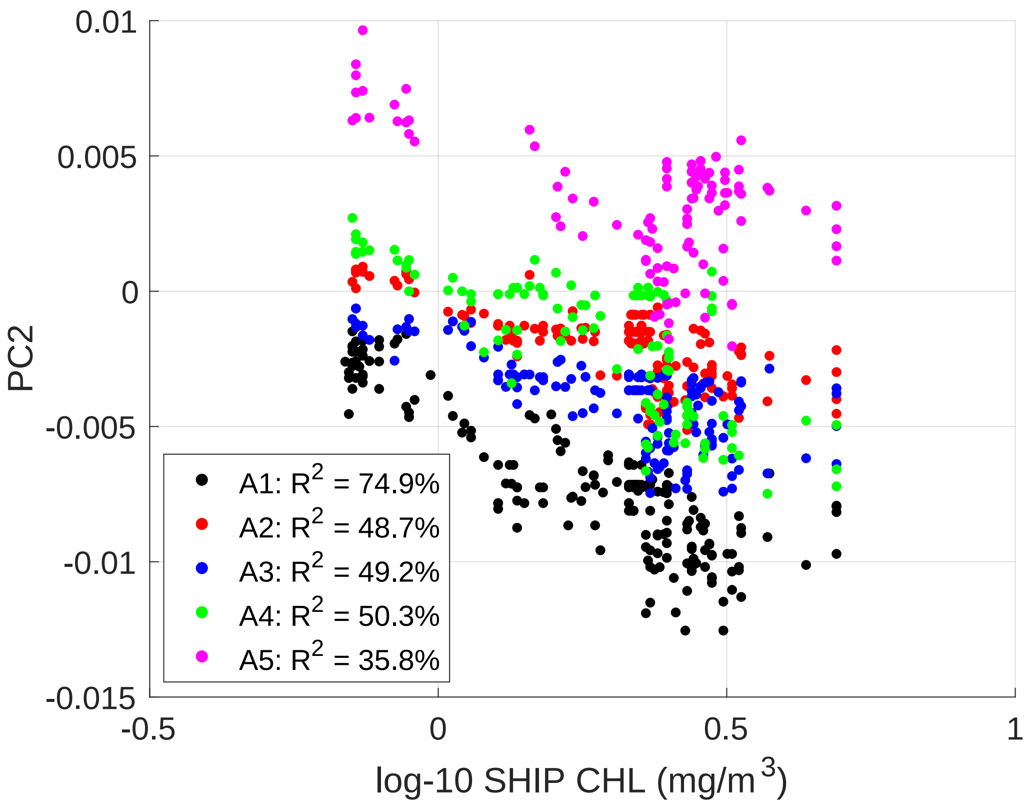

Figure 2: PC2 plotted against log-10 ship-based chl-a for lines A1, A2, A3, A4, and A5. Points colored by transect.

5 Figure S3

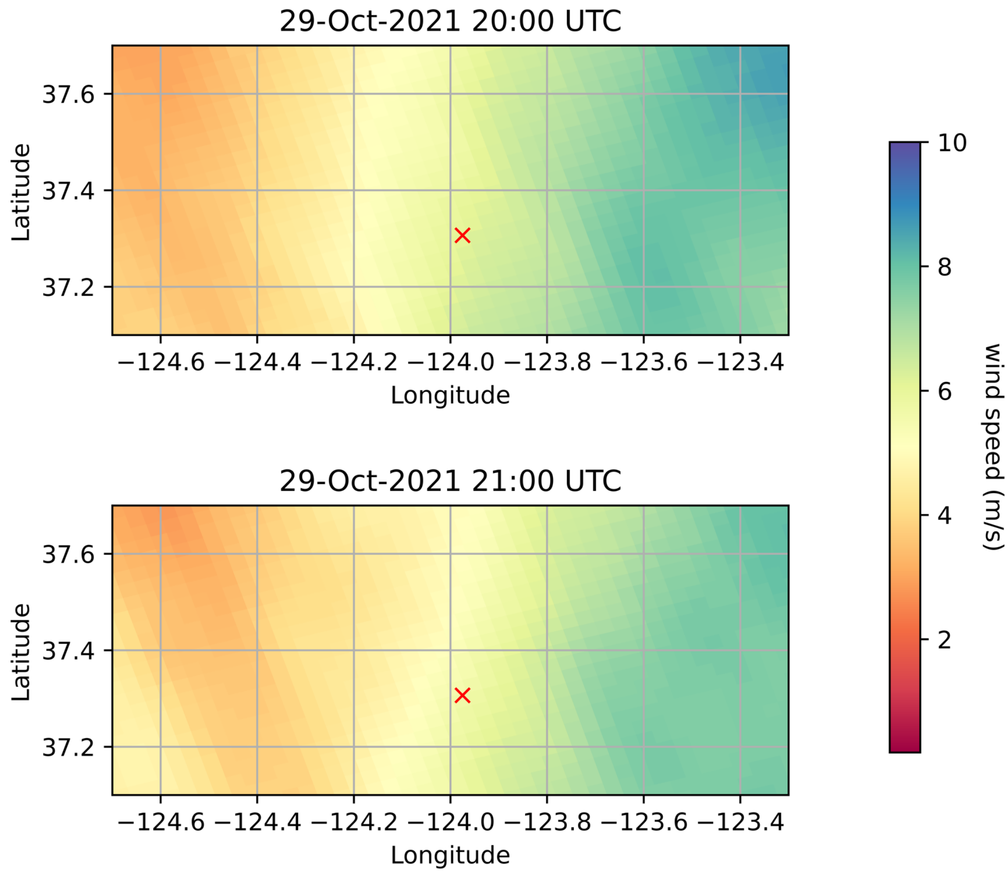

Figure 3: 3-km High-Resolution Rapid Refresh (HRRR) winds (Blaylock et al., 2018; Blaylock et al., 2017). Red x denotes approximate location of F2.

References

Blaylock, B. K., Horel, J. D., and Galli, C. (2018). High-resolution rapid refresh model data analytics derived on the open science grid to assist wildland fire weather assessment. *Journal of Atmospheric and Oceanic Technology*, 35(11):2213 – 2227. https://doi.org/10.1175/JTECH-D-18-0073.1.

Blaylock, B. K., Horel, J. D., and Liston, S. T. (2017). Cloud archiving and data mining of high-resolution rapid refresh forecast model output. *Computers Geosciences*, 109:43–50. https://doi.org/10.1016/j.cageo.2017.08.005.